

A plausible link between dynamically unsettled molecular gas and the radio jet in NGC 6328

M. Papachristou^{1,2}, K.M. Dasyra^{2,1}, J.A. Fernández-Ontiveros^{1,3,4}, A. Audibert^{1,5,6}, I. Ruffa^{7,1}, F. Combes⁸, M. Polkas¹, A. Gkogkou⁹

¹ National Observatory of Athens (NOA), Institute for Astronomy, Astrophysics, Space Applications and Remote Sensing (IAASARS), GR-15236, Greece

² Department of Astrophysics, Astronomy & Mechanics, Faculty of Physics, National and Kapodistrian University of Athens, Panepistimiopolis Zografou, 15784, Greece

³ Istituto di Astrofisica e Planetologia Spaziali (INAF-IAPS), Via Fosso del Cavaliere 100, I-00133 Roma, Italy

⁴ Centro de Estudios de Física del Cosmos de Aragón (CEFCA), Plaza San Juan 1, E-44001, Teruel, Spain

⁵ Instituto de Astrofísica de Canarias, Calle Vía Láctea, s/n, E-38205, La Laguna, Tenerife, Spain

⁶ Departamento de Astrofísica, Universidad de La Laguna, E-38206, La Laguna, Tenerife, Spain

⁷ Cardiff Hub for Astrophysics Research & Technology, School of Physics & Astronomy, Cardiff University, Queens Buildings, The Parade, Cardiff, CF24 3AA, UK

⁸ Observatoire de Paris, LERMA, Collège de France, CNRS, PSL Univ., Sorbonne Univ., F-75014 Paris, France

⁹ Aix Marseille Univ., CNRS, CNES, LAM, Marseille, France

ABSTRACT

We report the detection of outflowing molecular gas at the center of the nearby radio galaxy NGC6328 ($z=0.014$), which has a gigahertz-peaked spectrum radio core and a compact (2 pc) young double radio lobe tracing jet. Utilizing Atacama Large Millimeter/submillimeter Array (ALMA) CO(3 – 2) and CO(2 – 1) observations, as well as a novel code developed to fit the 3D gas distribution and kinematics, to study the molecular gas kinematics, we find that the bulk of the gas is situated within a highly warped disk structure, most likely the result of a past merger event. Our analysis further uncovers, within the inner regions of the gas distribution ($R < 300$ pc) and at a position angle aligning with that of the radio jet (150°), the existence of two anti-diametric molecular gas structures kinematically detached from the main disk. These structures most likely trace a jet-induced cold gas outflow with a total lower limit mass of $2 \times 10^6 M_\odot$ mass, corresponding to an outflow rate of $2 M_\odot \text{ yr}^{-1}$ and a kinetic power of $2.7 \times 10^{40} \text{ erg s}^{-1}$. The energy required to maintain such a molecular outflow is aligned with the mechanical power of the jet.

Key words. galaxies: ISM – galaxies: Individual: NGC6328 – galaxies: jets – galaxies: kinematics and dynamics – galaxies: active

1. Introduction

A central question in the study of galaxy evolution is the role and importance of the central engines of active galaxies, active galactic nuclei (AGN), in regulating star formation (SF). As a supermassive black hole (SMBH) grows in the center of galaxies, due to the accretion of gas (Antonucci 1993), it releases energy in the form of radiation pressure or in the form of radio jets (i.e., collimated plasma that is often relativistic). This energy can be coupled to the surrounding interstellar medium (ISM), affecting the molecular gas that is essential for SF (Krumholz et al. 2009). Thus, AGN feedback can suppress gas accretion and quench SF, ultimately shaping the evolution of the host galaxy (Croton et al. 2006; Sijacki et al. 2007; Harrison et al. 2018).

The role of relativistic jets in AGN feedback has primarily been recognized through their ability to heat the circumgalactic environment and prevent gas cooling and inflows by inflating thermal bubbles (so-called "maintenance mode" feedback) (e.g., Fabian 2012; McNamara & Nulsen 2012). Alternatively, simulations have shown that jets can also be highly efficient at coupling their power to the local dense medium as they propagate through the ISM, providing a source of shocks and ram pressure and inducing turbulence (Wagner & Bicknell 2011; Wagner et al.

2012; Mukherjee et al. 2016; Mukherjee et al. 2018). When the clouds are dissipated to very hot and tenuous conditions, or even accelerated to velocities greater than the escape velocity of the gravitational potential, SF declines as the galaxy is starved of its star-forming fuel. This has been observed in simulations in the aforementioned studies, although only a small fraction of the ISM can reach such high velocities and most of the gas will eventually fall back in a galactic fountain. Also, according to the simulations, the total impact a jet will have on the surrounding gas depends on numerous parameters, mainly its power and orientation relative to the gas disk and the clumpiness of the disk. Powerful jets ($\sim 10^{45} \text{ erg s}^{-1}$) tend to drill easily through the ISM and escape to intergalactic space much faster than low-power jets ($\sim 10^{43} \text{ erg s}^{-1}$). Low-power jets get diffused in the dense gas environment for larger timescales. As a result they tend to power high-pressure bubbles, greatly affecting the ISM (Talbot et al. 2022; Mukherjee et al. 2016).

Recent studies have shown that compact radio sources, associated with low-powered parsec-scale young radio jets are quite common (Baldi et al. 2018, 2021). Young jets have been also associated with peaked-spectrum (PS) radio sources (O’Dea & Saikia 2021) which exhibit a characteristic turnover in their radio spectral energy distribution (SED) due to their interaction with the

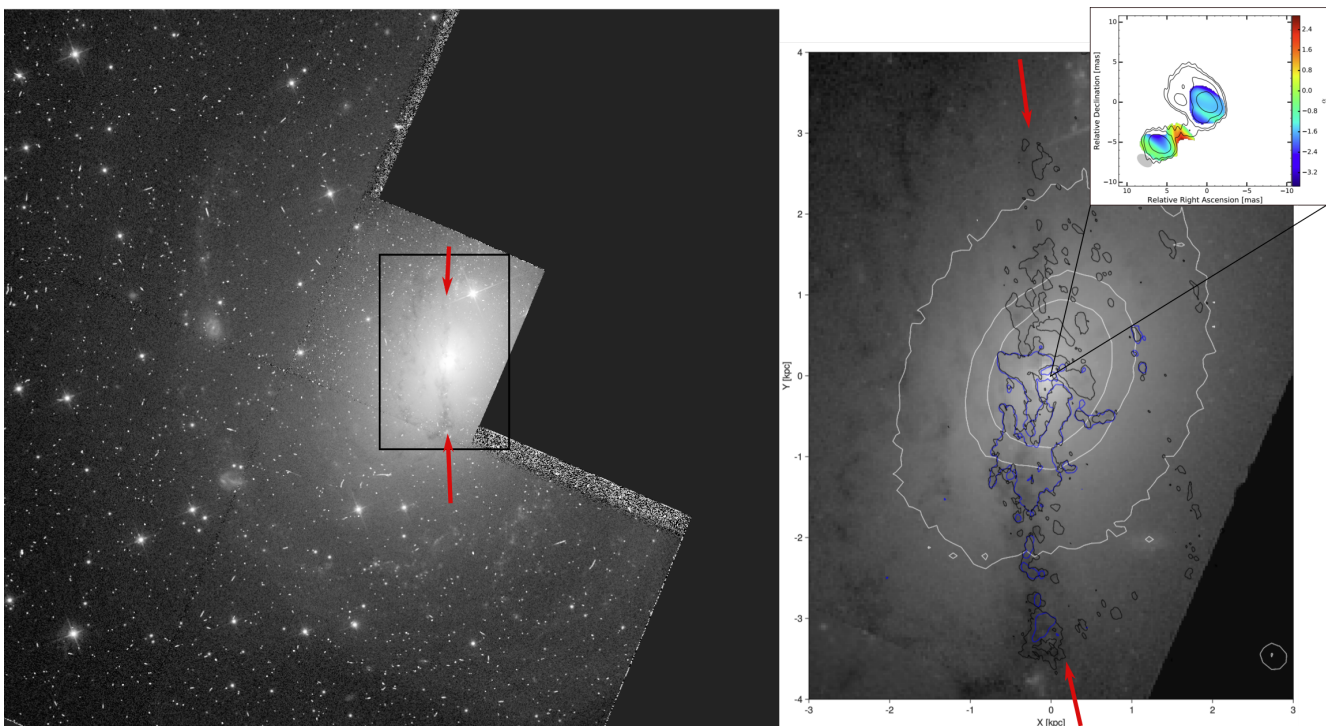


Fig. 1: Hubble Space Telescope (WFPC2) view of NGC6328. Left: Grand-scale (~ 16 kpc) image (obtained from [Wikimedia](#)). Right: Zoomed-in view of the central 4 kpc (indicated also in the black box on the left). CO(2 – 1) (black) and CO(3 – 2) (blue) 4σ contours of the maximum flux per channel. The central north-south oriented dust lane, correlated with the CO emission, is indicated with red arrows, along with a less prominent feature to the west marking the start of a faint spiral arm. The elliptical contours represent the stellar distribution from VLT in the J band. In the top right inset, we include the bipolar radio map from [Angioni et al. \(2019\)](#) and the spectral index between 8.4 GHz and 22.3 GHz.

ISM. There are two proposed mechanisms to which the observed peak can be attributed, namely the free-free absorption (FFA) of the synchrotron radiation by the ionized, shocked, and dense ISM ([Bicknell et al. 1997](#)) and synchrotron self-absorption (SSA) ([Kellermann & Pauliny-Toth 1969](#)). Radio spectra obtained from simulations of young jet-ISM interactions ([Bicknell et al. 2018](#)) reproduce the observed turnover frequency and radio source size correlation. This makes PS sources suitable candidates for understanding the impact of young jets in the ISM and their significance in AGN feedback.

NGC 6328 is an early-type galaxy with a well-studied gigahertz-peaked source (GPS) radio core (PKS B1718-649) that exhibits clear evidence of out-of-dynamic-equilibrium kinematics in both its cold and warm gas phases ([Maccagni et al. 2014, 2016b, 2018](#)). Due to its proximity ($D = 62.88$ Mpc at $z = 0.014$), NGC6328 is an ideal target for studying the impact of young jets on the ISM with the Atacama Large Millimeter/submillimeter Array (ALMA) and it is part of the CO-ARC survey on the molecular gas content of radio galaxies ([Audibert et al. 2022](#)).

PKS B1718-649 shows a typical GPS spectrum, with a turnover point at around 3.2 GHz ([Tingay et al. 1997](#)). The radio spectrum is best modeled with the FFA model ([Tingay et al. 1997](#)), while close monitoring of the source reveals significant variability, likely due to a mixture of intrinsic processes associated with the dense local environment and adiabatic losses of the synchrotron-emitting lobes ([Tingay et al. 2015](#)). High-resolution (~ 0.3 pc) very long baseline interferometry (VLBI) observations resolve the source into a bipolar structure, with the two lobes being separated by a projected distance of ~ 2 pc ([Tingay et al. 1997; Tingay & de Kool 2003](#)). The spectral index (see Figure 1

inset) between 8.4 GHz and 22.3 GHz suggests that the core of the young radio source is strongly absorbed in these frequencies, and is located between the two lobes. The structure is unresolved in lower-resolution ($29.7''$ or 8.7 kpc) observations at 1.4 GHz from the Australia Telescope Compact Array (ATCA), in which the total measured flux (3.98 Jy) is comparable with the VLBI emission ([Maccagni et al. 2014](#)).

Particularly interesting is the warped and complex kinematics and structure of the cold gas disk ([Maccagni et al. 2014](#)), which is indicative of an external accretion event from an initially misaligned disk (see e.g., [van de Voort et al. 2015; Ruffa et al. 2019](#)). This event could provide valuable insights into the feeding mechanism of the AGN and the transport of angular momentum in galaxy disks. This complex structure is also visible in the dust distribution seen in Hubble Space Telescope (HST) observations through the Wide Field and Planetary Camera 2 (WFPC2), where it appears as a near edge-on north-south oriented dust lane in the central $23''$ of the bulge. At larger distances, faint spiral features of dust and stars are also evident, resembling a more face-on disk orientation. This is prominent in the Neil Gehrels Swift Observatory maps obtained using Ultraviolet/Optical Telescope (UVOT) filters (UVM2 at 2246 \AA and UVW2 at 1928 \AA). Overall, the optical surface brightness of NGC6328 is dominated by a sersic $1/4$ elliptical bulge with a position angle (PA) of 145° and an axis ratio (b/a) of 0.72 ([Veron-Cetty et al. 1995](#)).

Observations of atomic hydrogen in NGC 6328 by [Maccagni et al. 2014](#) revealed a massive HI disk with a total mass of $M_{\text{HI}} = 1.1 \times 10^{10} M_\odot$. Similar to the molecular gas, the kinematics of the HI disk can be modeled as a warped disk, with an almost constant

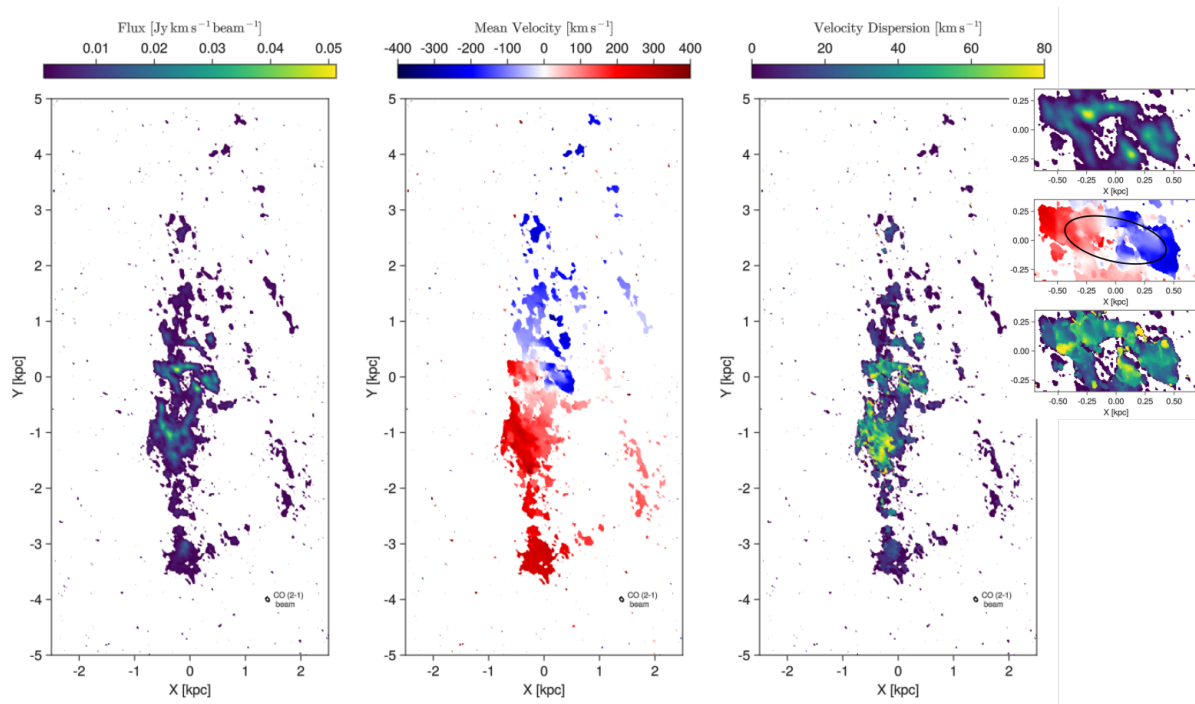


Fig. 2: From left to right: Zeroth, first, and second moments of the CO(2 – 1) emission. The ellipse in the lower right corner of each panel represents the observational beam. The inset on the right provides a zoomed-in view of the central inner disk-like structure, also highlighted by a black ellipse.

circular velocity of 220 km s^{-1} . In the central $30''$ (or 8.5 kpc for the adopted Lambda cold dark matter (ΛCDM) cosmology with $H_0 = 69.32 \text{ km s}^{-1} \text{ Mpc}^{-1}$, $\Omega_m = 0.29$, $\Omega_\Lambda = 0.71$), the disk is highly inclined, with an inclination angle, i , of $\sim 90^\circ$, and oriented along the PA of the observed dust lane (180°). In outer regions, up to $80''$ (or 23 kpc), the disk slowly warps to a face-on geometry ($i = 30^\circ$ and $\text{PA} = 110^\circ$), consistent with the galaxy’s spiral features. Further out (past the $80''$ radius), asymmetric features are present northwest and south of the disk. These deviate from regular rotation and are attributed to an ongoing merger or interaction (Veron-Cetty et al. (1995), Maccagni et al. (2014)

Very Large Telescope (VLT) Spectrograph for INtegral Field Observations in the Near Infrared (SINFONI) observations of warm molecular hydrogen at $2.12 \mu\text{m}$ (1-0) S(1) and $1.95 \mu\text{m}$ (1-0) S(3) by Maccagni et al. (2016a) showed H_2 emission within the central 700 pc of the galaxy following a nearly edge-on inner disk at a PA of 85° , almost perpendicular to the dust lane. The H_2 at an excitation temperature of $1100 - 1600 \text{ K}$ has an estimated mass of $10^4 M_\odot$. In the outer disk, two warm H_2 blobs have been detected in opposite directions, at a projected distance of $1 - 1.5 \text{ kpc}$, close to the radio jet axis. This axis happens to be nearly parallel to the major axis of the stellar isophote curves ($\text{PA} \sim 150^\circ$).

In this paper, we present a new kinematic analysis of the molecular gas in NGC 6328, utilizing previous CO(2-1) observations (Maccagni et al. 2018) and more recent CO(3-2) data obtained with ALMA. The paper is structured as follows: Section 2.1 provides a description of the ALMA observations. In Section 3, we present our novel approach to the kinematic modeling of the cold gas disk of the galaxy and the optimal 3D model that describes its structure. There, emphasis is given to the nature of the clouds that strongly deviate from the optimal model in the form of outflowing gas. Finally, in Section 5, the possi-

ble connections of the outflows with the AGN and the jet are discussed.

2. Observations

2.1. ALMA data reduction

NGC6328 was observed using ALMA Band 6 at a rest frame frequency, ν_{rest} , of 230.5 GHz (project ID: #2015.1.01359.S, PI: F. Maccagni) in September 2016, and using Band 7 at $\nu_{\text{rest}} = 345.8 \text{ GHz}$ (project ID: #2017.1.01638.S, PI: S. Kamenno) in January 2018. The phase center of the observations was the position of the nucleus ($\delta_{\text{RA}} = 17:23:41.03$ and $\delta_{\text{DEC}} = -65:00:36.615$), with a single pointing covering a field of view (FoV) of $25''$ in Band 6 and $18''$ in Band 7.

The ALMA Band 6 observations were carried out with 39 12-m antennas and an extended array configuration with baseline lengths ranging from 15 to 2483 m. The on-source integration time was 1.85 hours. The correlator setup was selected to center the CO(2-1) line with a velocity range of $\pm 1200 \text{ km/s}$ in the 1.86 GHz bandwidth and a channel width of 7.8 MHz (20 km s^{-1}).

The data were calibrated using the Common Astronomy Software Applications package (CASA) (McMullin et al. 2007), version 4.7, and the calibration scripts provided by the ALMA archive. J1617-5848, J2056-4714, and J1703-6212 were respectively used as flux, bandpass, and phase calibrators, resulting in 15% accuracy. The data were imaged using the CASA `tclean` task with Briggs weighting and a robust parameter of two, in order to maximize the sensitivity, resulting in a synthesized beam of $0''.27 \times 0''.19$ at $\text{PA} = 33.75^\circ$. The images were binned to a 20 km s^{-1} (15.2 MHz) spectral resolution and corrected for primary beam attenuation.

The continuum map was made using natural weighting, resulting in a signal-to-noise ratio (SNR) of 400. After five itera-

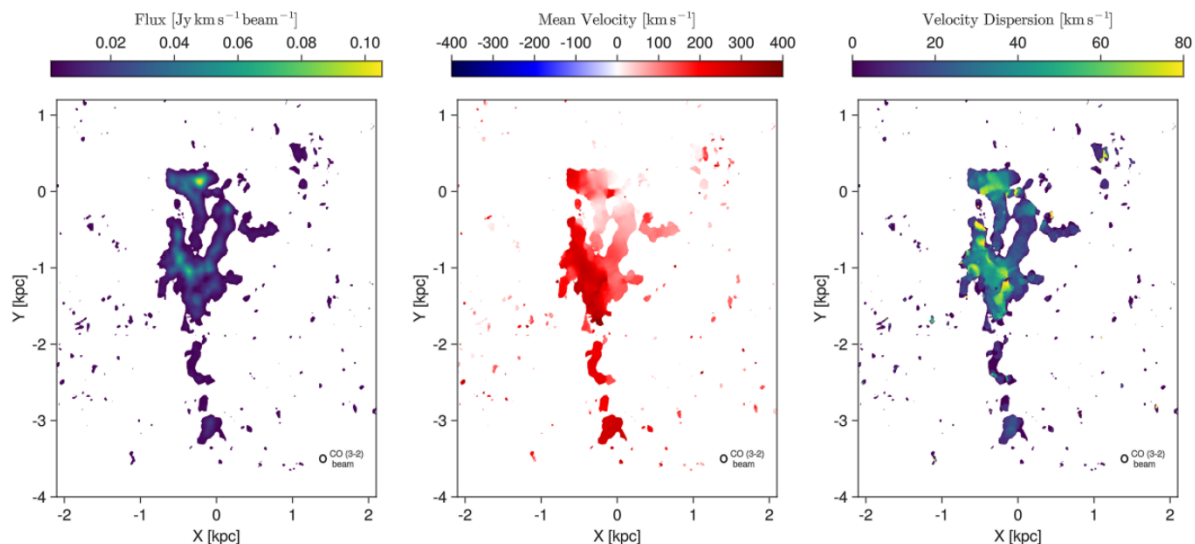


Fig. 3: From left to right: Zeroth, first, and second moments of the CO(3 – 2) emission. The black ellipse represents the beam of the observation. Due to spectral coverage limitation, only the positive velocities are observed, and thus only the redshifted part of the disk is visible.

tions of phase-only self-calibration and one iteration amplitude and phase self-calibration, the SNR was raised to 7912 with an rms of 0.04 mJy/beam. The restoring beam is $0''.194 \times 0''.107$ at $PA = 21.5^\circ$. In the continuum map the radio source is unresolved. The CO(2 – 1) line emission cube was obtained after subtraction of the continuum in the line-free channels with the CASA task `uvcontsub`. The rms noise was estimated at 0.04 mJy/beam, with a restoring beam of $0''.272 \times 0''.186$ at $PA = 34.8^\circ$.

The ALMA Band 7 observations were carried out with 44 antennas and baselines ranging from 15 to 1400m. The shortest baseline provides a larger recoverable angular scale of about $11''$. The total integration time was 44.7 minutes. The galaxy was observed in dual-polarization mode with 2 GHz total bandwidth and 128 channels per spectral window (SPW), corresponding to $\sim 13.7 \text{ km s}^{-1}$ velocity resolution. The choice of the tuning setup was to provide simultaneous observations of CO(3 – 2), HCO⁺(4-3), and CS(7-6) emission lines, and therefore the SPW of the CO(3 – 2) line emission did not center the observed frequency of the CO(3 – 2) line, missing out the negative velocities. The data reduction was performed using CASA version 5.4.0-70. For the phase and bandpass calibrations, J1703-6212 and J1647-6438 were used, respectively. The flux was calibrated using J1427-4206, assuming that at 350GHz the flux density is 2.19 Jy (for a spectral index of -0.52), resulting in an accuracy of 8%. The continuum map was made using the CASA `tclean` task with natural weighting, resulting in a SNR of 186. After five iterations of phase-only self-calibration, and one iteration of amplitude and phase self-calibration, a SNR of 5063 was reached, with an rms of 0.044 mJy/beam and a restoring beam of $0''.339 \times 0''.269$ at $PA = 6.9^\circ$. After subtracting the continuum and cleaning using the same criteria as in Band 6, we obtained a CO(3 – 2) data cube with a restored beam of $0''.320 \times 0''.275$ at $PA = 2.2^\circ$, and an rms noise of 0.297 mJy/beam per channel of 20 km s^{-1} .

2.2. Ancillary data

We also used archival ancillary data from the X-shooter instrument on the VLT, which provides simultaneous coverage of

the optical and near-infrared spectral ranges. These data (PI: Maccagni and program name: 105.20QD.001) have not yet been published. They have only been publicly released and calibrated through the standard pipeline. We used the X-shooter data to present the basic ionized gas properties of NGC 6328, particularly in the central regions of the galaxy. While a detailed analysis of these data is beyond the scope of this paper, we note that they provide valuable complementary information to the ALMA data analysed here, and will be discussed in more detail in future works.

3. A new, physically motivated 3D fitting Bayesian tool for the gas kinematics and distribution model

To investigate the kinematics of the molecular gas in NGC6328, we developed a novel Bayesian tilted-ring code that extracts the galaxy’s intrinsic 3D structure from observational data. Tilted-ring models are common in kinematic studies, modeling galaxies either in two dimensions (through average velocity moment maps) or in three dimensions (observational cubes), with ^{3D}BAROLO being a notable example (Teodoro & Fraternali 2015). Traditional tilted-ring models, however, typically either treat each ring as an isolated entity or connect them using simple interpolation schemes, without accounting for the physical interactions between adjacent rings. Recognizing that the molecular gas in NGC6328 is likely part of a strongly warped structure, arising from a differential precession process due the presence of a nonspherical potential, our code incorporates additional physical principles to depict the galaxy’s 3D structure and its temporal evolution in a more interconnected manner. This method provides a coherent connection between rings, which is especially crucial in the context of warped structures, and which helps mitigate parameter degeneracies related to overfitting. This is particularly beneficial in regions where distinct parts of the disk with different intrinsic rotation velocities overlap in projection. As a result, our approach enhances the reliability of inferences regarding the disk’s kinematics and geometry.

Additionally, our code includes an alternative model that employs the traditional interpolation schemes for the rings' geometrical properties in the galaxy plane, akin to traditional methods. This alternative model is initialized using the resulting geometry derived from the physically motivated model, but allows for more flexibility in case the physical model might be overly constraining or not fully applicable. We start by describing this latter setup of our model.

3.1. Generic tilted-ring model

Our model starts by constructing the galaxy's disk as a series of concentric circular rings. The orientation of each ring within the galaxy's coordinate system, for a given radius, r , is determined by two angles: its polar angle, $\theta(r)$, and a modified azimuthal angle termed as the longitude of ascending node (LON), $\lambda(r)$. The LON specifies the point where the ring intersects the x, y plane of the galaxy's coordinate system. Consequently, the normal vector to the plane of the ring, which is also indicative of the direction of the ring's angular momentum, is given by

$$\hat{n}(r) = \begin{pmatrix} -\sin \theta(r) \sin \lambda(r) \\ \sin \theta(r) \cos \lambda(r) \\ \cos \theta(r) \end{pmatrix}. \quad (1)$$

The derived $\theta(r)$ and $\lambda(r)$ of each ring are then transformed into the observable inclination, $i(r)$, and PA, $PA(r)$, using a reference "ring" for the main axis of the potential (i_{Bulge} and PA_{Bulge} ; see Appendix B).

For the rotation curve, $V_C(r)$, we used a gravitational potential comprised of three components: a SMBH, a bulge, and a dark matter halo. Further components (such as a molecular gas disk) can be provided to the code, but in the case of NGC6328 its mass is too small to significantly influence the kinematics. For the SMBH, we used a mass of $4.1 \times 10^8 M_\odot$ (Willett et al. 2010). For the dark matter halo component, we used the Navarro–Frenk–White profile (Navarro et al. 1996), with both the virial mass and the concentration parameter as free parameters (using the parameterization of Bullock et al. 2001). For the bulge component, we utilized a Hernquist potential (Hernquist 1990). We assumed that noncircular velocities are negligible.

The best solution of the model is determined in a Bayesian framework. The model aims to maximize the likelihood that the predicted line-of-sight velocities (V_{LOS}) are consistent with the observed V_{LOS} for all molecular gas clumps detected in the ALMA data at the same position in the sky.

To determine which observed clouds are reliably detected, we used a clump detection algorithm (see Appendix A) for the ALMA cube. Then, given the set of N observable molecular clouds with sky projected coordinates $\{(x_n, y_n, V_n)\}_{n=1}^N$, the code calculates for every cloud the minimum spatial distance (in sky coordinates) from every ring of our geometrical model. If this distance is below a critical limit (i.e., comparable with the beam size), the code calculates the projected velocity difference, $\delta V_{nk} = |V_n - V_{\text{los}}(\phi_{\text{closest}}, V_{ck}, i_k, \phi_{0k})|$, with ϕ_{closest} corresponding to the closest spatial position on the projected ellipse of the k ring. When δV is calculated for all the possible neighbouring rings, the code assigns the smallest one to the cloud, m , so $\delta V_n = \min(\delta V_{nk})$. Assuming a Gaussian likelihood of observing these velocity differences, we maximize the log-likelihood of

$$\log L_{\text{ALMA}}(\{\delta V_n\}_1^N | \bar{\theta}) = -\frac{1}{2} \left(\sum_{n=1}^N \frac{\delta V_n^2}{\sigma_V^2} + N \log(2\pi\sigma_V^2) \right), \quad (2)$$

where σ_V is a measure of the dispersion of the clouds' velocity from a perfectly rotating disk.

For a more precise estimation of the large-scale kinematics we also incorporated HI rotational velocity data points from Veron-Cetty et al. (1995) and Maccagni et al. (2014), using them as a second likelihood distribution together with the ALMA data. We selected the HI data points only for the outer part of the galaxy in order to avoid any influence of the warp. This provides us with better accuracy on the dark matter component of the model, and thus a more accurate description of the overall velocity curve.

The total posterior distribution was constructed using the joint likelihood distribution of the observable data with prior information regarding the stellar distribution and mass from Maccagni et al. (2016b), as well as the specific geometric constraints of the disk from the dust distribution and the shape of the HI disk mentioned in Section 1. The best set of parameters was estimated by sampling the posterior distribution using a Markov Chain Monte Carlo (MCMC) code (Vesselinov & O'Malley 2013).

3.2. Physically connected ring model

In the case of rings that are physically connected, the fitting procedure remains identical, with the exception that the geometrical properties of the disk, $\theta(t, r)$ and $\lambda(t, r)$, are time-dependent, and their evolution is governed by the precession induced by a nonspherical potential.

In a nonspherical potential, it is widely accepted that the gas will precess due to the torques induced by the gravitational potential of the stars, until it eventually relaxes back into alignment with one of the preferred axes, commencing either clockwise or counterclockwise rotation. Rings at smaller radii precess more rapidly due to their higher angular velocity, which leads to a warped disk structure. The differences in angular velocity and precession rates between neighboring rings generate internal torques. These internal torques serve as dissipative forces, promoting the alignment of each ring with its neighbors and eliminating the component of the gas's angular momentum that is perpendicular to the stellar angular momentum direction, and thus facilitating the settling of the gas to the potential's preferred axes. Over time, these processes result in the alignment or counter-alignment of the gas with the stellar angular momentum. This alignment occurs over timescales ranging from hundreds of millions to billions of years (Tohline et al. 1982; Lake & Norman 1983; Steiman-Cameron & Durisen 1988; Sparke 1996; Davis & Bureau 2016).

Assuming that precession is slow compared to the time taken for one complete orbit, the change in the orbital orientation (denoted as $\hat{n}(t, r)$) due to the asphericity of the galaxy and viscous forces can be calculated by averaging the torque induced over an orbital motion as follows:

$$\frac{d\theta}{dt} = -\frac{T_\theta}{h \sin \theta} - f_\theta(t, r, \theta, \lambda) \quad (3)$$

$$\frac{d\lambda}{dt} = \frac{T_\lambda}{h \sin \theta} \quad (4)$$

where $T_{\theta, \lambda} = -\frac{\partial \langle \Phi \rangle(r, \theta, \lambda)}{\partial (\lambda, \theta)}$ represents the torques exerted on the ring in the θ and λ directions due to the asphericity of the potential, Φ , and $h(r) = rV_C(r)$ is the orbital angular momentum per unit mass. The rotation curve, $V_C(r)$, is computed in the same manner as in the generic model, as described in the previous section. The quantity, $\langle \Phi \rangle(r, \theta, \lambda)$, denotes the gravitational potential averaged along the circular orbit as $\langle \Phi \rangle(r, \theta, \lambda) = \frac{1}{2\pi} \oint_{r, \theta, \lambda} \Phi d\phi$, where $0 \leq \phi \leq 2\pi$.

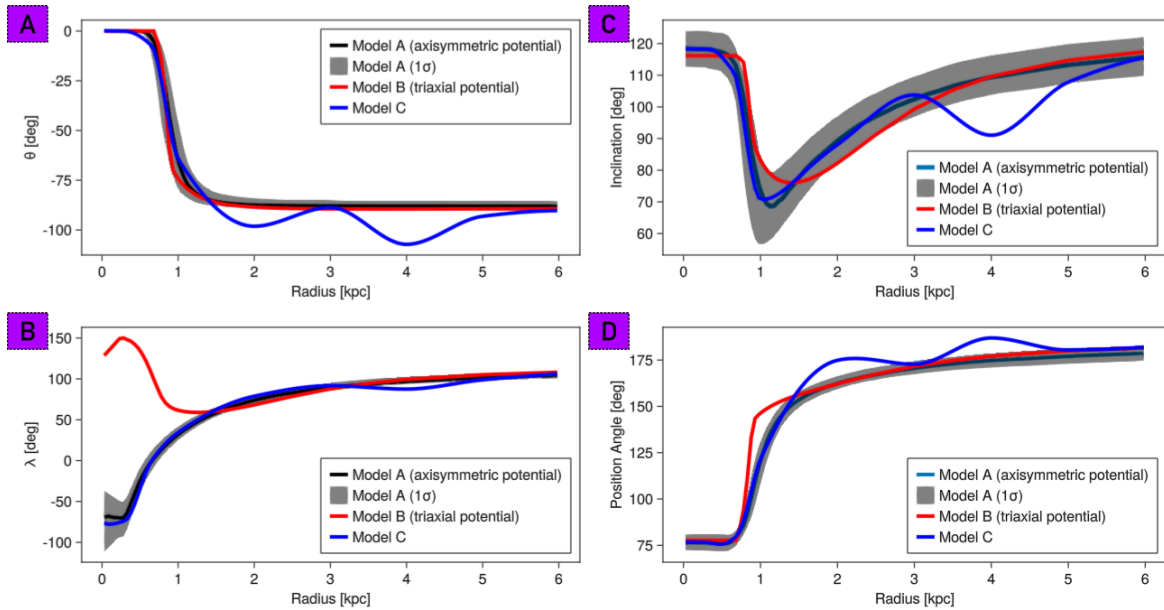


Fig. 4: Modeling results: Main geometrical parameters as function of radius. The gray band represents the 1σ confidence level of the parameters' posterior distribution regarding the axisymmetric model. **A:** Azimuthal angle of the disk in the galaxy coordinates, **B:** Line of nodes in the galaxy coordinates, **C:** Inclination, **D:** PA.

The function, $f_\theta(t, r, \theta, \lambda)$, represents the effect of viscous forces arising from the interaction between adjacent rings. For the evolution of the polar angle (tilting), as described in equation 3, we employ the dissipative force definition from [Steiman-Cameron & Durisen \(1988\)](#) to define the quantity

$$f_\theta(t, r, \theta, \lambda) = \frac{3 \sin 2\theta}{2} \frac{t^2}{t_e^3} \quad (5)$$

where t_e is the timescale required for the gas to settle.

This timescale is dependent on the geometric and physical characteristics of each ring and its neighbors. In their work, the authors approximated the inner torques between adjacent rings as resulting from viscous transport of angular momentum, through cloud-cloud collisions, computing t_e via the gas viscosity and higher-order derivatives. In this study, we used the simple approach of [Tohline et al. \(1982\)](#), who defines $t_e = \frac{\alpha}{|\dot{\lambda}(r) - \dot{\lambda}_0|}$, with the dot representing the time derivative. This method is based on the observation that the gas will have settled once it has precessed through an angle, α , around the main axis. While the original work by [Tohline et al. \(1982\)](#) used $\alpha = \pi/2$, we have chosen to treat this as a fitting parameter.

Equation 4 describes the precession of the disk (twisting). In the stress-free approximation, the effect of dissipative forces on twisting is considered negligible compared to their effect on tilting ([Steiman-Cameron & Durisen 1988](#)).

The potential that provides the necessary asymmetries for the above precession is assumed to be that of the bulge. Thus, we used a modified Hernquist bulge for the stellar density with total stellar mass M and scale lengths r_a, r_b , and r_c (in case of an axisymmetric bulge $r_a = r_b$), which is defined as

$$\rho_h(\mu) = \frac{M}{2\pi abc} \frac{1}{\mu(1+\mu)^3} \quad \text{where} \quad \mu^2 = \frac{x^2}{r_a^2} + \frac{y^2}{r_b^2} + \frac{z^2}{r_c^2} \quad (6)$$

From this we get the potential for every position, x, y, z , using the method of ellipsoidal shells ([Chandrasekhar 1969](#); [Binney & Tremaine 2008](#)),

$$\Phi_{\text{bulge}}(\xi) = -\frac{GM}{2} \int_0^\infty \frac{du}{\sqrt{r_a^2 + u} \sqrt{r_b^2 + u} \sqrt{r_c^2 + u} [1 + \xi(u)]^2} \quad (7)$$

where

$$\xi^2(u) = \frac{x^2}{r_a^2 + u} + \frac{y^2}{r_b^2 + u} + \frac{z^2}{r_c^2 + u} \quad (8)$$

The total chain of integration and differentiation processes were computed with the state-of-the-art auto-differentiation capabilities of the Julia language ([Bezanson et al. 2015](#)) using the ForwardDiff.jl ([Revels et al. 2016](#)) and quadgk.jl ([Johnson 2013](#)) packages. The equations were solved using the DifferentialEquations.jl package ([Rackauckas & Nie 2017](#)).

4. Results

4.1. Basic data products

The integrated CO(2-1) emission consists mainly of a highly inclined, disk-like structure extending out to $15''$. This distribution is spatially correlated with the dust absorption visible in Figure 1. The main disk structure is clumpy and asymmetric with respect to the center of the galaxy, with 66% of the total intensity belonging to the southern part of the disk and concentrated in an area 1.3 kpc^2 wide, around 1 kpc southwest of the center (30% of the total intensity).

The total integrated intensity is estimated to be $\Delta V = 165 \text{ Jy kms}^{-1}$, where we did not include flux below three times the local rms noise level. We estimate the total line luminosity using the [Solomon & Vanden Bout \(2005\)](#) formula:

$$L'_{\text{CO}(2-1)} = 3.25 \times 10^7 \frac{\Delta V D_L^2}{v_{\text{CO}(2-1)}^2 (1+z)^3} \quad [\text{K kms}^{-1} \text{ pc}^2] \quad (9)$$

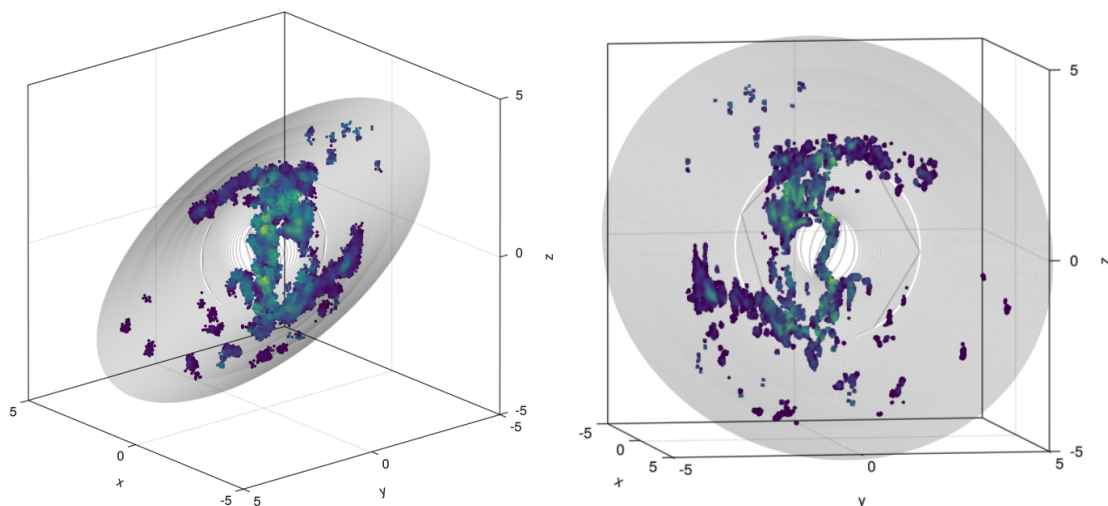


Fig. 5: 3D distribution of the CO(2 – 1) and CO(3 – 2) cloudlets and tilted ring of the model A at two random observable orientations. The X and Y axes represent the δ_{RA} and δ_{DEC} sky coordinates and the Z axis represents the line of sight. The color represents the integrated flux of each cloud. The axis units are in kpc.

where ν is the rest-frame CO(2 – 1) frequency in GHz, and D_L is the luminosity distance, which for $z = 0.014$ corresponds to $D_L = 62.88$ Mpc. This gives $L'_{\text{CO}(2-1)} = 3.28 \times 10^8 \text{ K km s}^{-1} \text{ pc}^2$.

From the integrated luminosity, we estimate the total molecular gas mass to be $1.8 \times 10^9 M_\odot$, using the relation $M_{\text{H}_2} = a_{\text{CO}} L'_{\text{CO}}$ (Solomon et al. 1997). We adopt a Galactic value of $4.6 M_\odot (\text{K km s}^{-1} \text{ pc}^2)^{-1}$ (Bolatto et al. 2013) for the conversion factor, a_{CO} , and a CO(2 – 1) to CO(1 – 0) flux ratio of four.

Based on the integrated intensity, first moment (mean velocity), and second moment (velocity dispersion) maps of the CO(2 – 1) and CO(3 – 2) lines (Figures 2 and 3), we identify multiple gas structures. In the inner regions, the presence of a bright molecular structure extending up to 650 pc is evident, with $i \approx 65^\circ$ and $\text{PA} = 72^\circ$, closely aligned with the warm H_2 emission (Maccagni et al. 2016b). This structure appears disk-like but could also resemble a ring.

The bulk of the molecular gas emission, however, is distributed in a main disk that is oriented north-south and highly inclined. The kinematics observed in the mean velocity map (Figure 2, middle panel) suggests the presence of a warp, as the PA clearly changes from 140° at 1.4 kpc to 180° at the maximum extent of 4 kpc. In the southwest portion of the disk, there is a massive substructure spanning an area of approximately 1.3 kpc^2 , centered at $\approx 1 \text{ kpc}$ from the center. This substructure has a mass of around $\sim 10^8 M_\odot$ (assuming $a_{\text{CO}} = 4.6 M_\odot (\text{K km s}^{-1} \text{ pc}^2)^{-1}$) and exhibits the maximum observed velocities (exceeding 350 km s^{-1}) and velocity dispersion (with values exceeding 80 km s^{-1}). A similar behavior can be observed in the opposite direction ($\text{PA} \approx -30^\circ$), though in much smaller and less massive clumps of molecular gas. Both of these regions coincide with notable H_2 regions outside of the inner disk (Maccagni et al. 2016b).

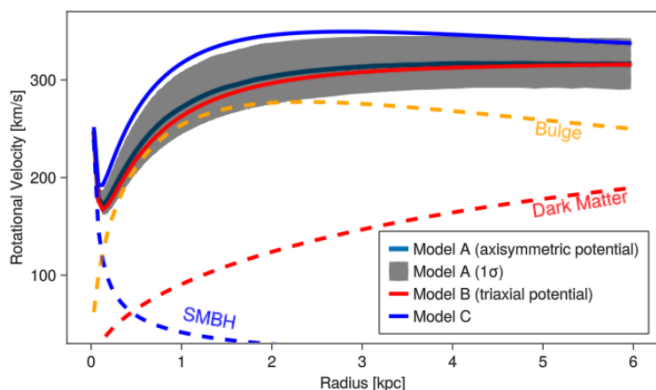


Fig. 6: Rotational velocity. The black line represents the best solution of the axisymmetric model, red the triaxial, and blue the generic interpolating model. The gray band represents the 1σ confidence level of the parameters' posterior distribution regarding the axisymmetric model.

4.2. Fitting the ALMA data cube with our 3D code

We used our new Bayesian code to fit the full ALMA cube and produce the galaxy's rotation curve for several assumptions. In models A and B, we used a physical model that describes the time-dependent evolution of a set of tilted rings within a triaxial axisymmetric modification of the Hernquist potential. The physical approach in models A and B captures the warped disk motion and structure, which results from gas infalling toward the gravitational potential, feeling torques from a nonspherical potential, and dissipative forces. In a third model, named C, we adopted the more generic assumptions mentioned in section 3.1.

For models A and B, there are 12 and 13 fittable parameters, respectively. These include the bulge stellar mass, the scale size on the three axes, r_a, r_b, r_c (for the axisymmetric model, $r_a = r_b$), the virial mass and concentration parameter of the dark matter component, the initial values of $\theta(0, r) = \theta_0$ and $\lambda(0, r) = \lambda_0$, the settling angle, α , the time elapsed from the initial configuration, τ , and the orientation of the reference ring ($i_{\text{Bulge}}, \text{PA}_{\text{Bulge}}$). The corner plot depicting the posterior distribution of the parameters for Model A is presented in Figure C.1.

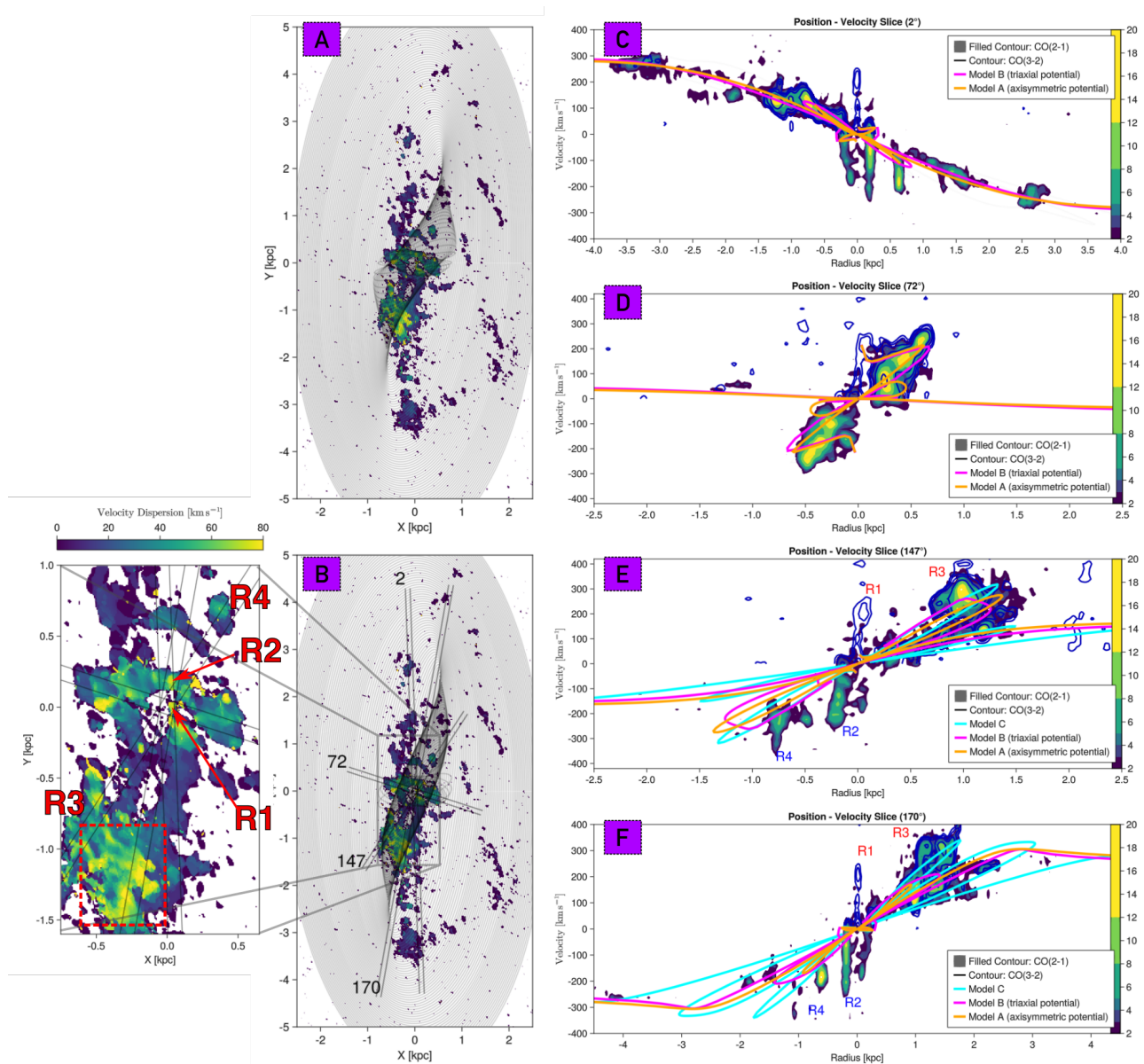


Fig. 7: Position velocity slices of CO(2-1) and CO(3-2) emission cubes. Panels A and B: Sky-projected tilted rings for the axisymmetric potential model (A) and the triaxial potential model (B) embedded on top of the CO(2-1) dispersion map. Panels C and D: Slices at angles of 2° and 72° , covering most of the gas emission and the major axes of the inner disk, respectively. Superimposed on these slices are the velocity projections of models A and B. Model C is omitted to avoid clutter, as its projected velocities are similar to those of the other models. The color map represents the SNR. Panels E and F: Position velocity slices along the PAs of 147° and 170° where we observe the maximum gas dispersion. Embedded in these slits are also the velocity projections of models A, B, and C.

For model C, $\theta(r)$ and $\lambda(r)$ were generated using an interpolated set of $N = 10$ pairs $(r_k, \theta_k, \lambda_k)$, which are fittable parameters. The rotation curve uses the same parameters as the other models, which are the bulge stellar mass, a scale size for the bulge, r_d , and the virial mass of the dark matter component, for a total of 26 parameters.

Panels A and B of Figure 4 show the resulting geometry in the galactic plane, characterized by the angles $\theta(t, r)$ and $\lambda(t, r)$, as defined in the previous section. Panels C and D of the same figure display the inclination and PA of the rings, as observed in the plane of the sky.

Given the resulting 3D structure, we can observe the molecular gas from an alternative viewpoint (Figure 5), where we see a spiral-like structure as the gas moves toward the central disk. In Figure 6 we present the rotational velocity and its components. The best-fitting geometrical parameters reveal that the disk has settled into a stable configuration within the central 600 pc (the inner disk) 100 – 400 Myrs after its initial configuration. Most of the emission observed in the inner disk is a result of the projection of multiple positions of the disk, with the primary contribution coming from the inner disk itself and a smaller contribution from the rapidly warping outer regions. This explains the observed velocity dispersion and the small asymmetry of the emission

Table 1: Resulting parameters for models A, B, and C.

Parameter	Model A	Model B	Model C
M_*	$1.7 \times 10^{11} M_\odot$	$1.6 \times 10^{11} M_\odot$	$2.1 \times 10^{11} M_\odot$
M_{vir}	$3.4 \times 10^{12} M_\odot$	$5.4 \times 10^{12} M_\odot$	$2.5 \times 10^{12} M_\odot$
r_a	2.26 kpc	2.7 kpc	2.1 kpc
r_b	2.26 kpc	2.26 kpc	-
r_c	2.54 kpc	2.4 kpc	-
θ_0	-87.8°	-89°	-
λ_0	112°	114°	-
α	60.6°	54.9°	-
c_{vir}	7.4	7.4	7.4
τ	120 Myrs	380 Myrs	-
i_{Bulge}	61.7°	63.8°	62°
PA_{Bulge}	257°	258°	257°

Notes. M_* is the bulge stellar mass, r_a , r_b , and r_c are the three axis scales and i_{Bulge} , PA_{Bulge} is the orientation of the axis, c , relative to the observer. M_{vir} is the virial mass and c_{vir} the concentration parameter of the dark matter. θ_0 and λ_0 are the starting values of the disk orientation. α is the dissipation settling angle and τ the time after the initial values.

along the inner disk's major axis. The orientation of the disk rapidly changes over the next ~ 1 kpc, with similar changes in the azimuthal angle reproduced by both the axisymmetric and the triaxial models due to the dominant diffusion term. However, the change in the longitude of the ascending node (λ) shows a different behavior in the two models, with the disk in the triaxial model shifting inward of 1.5 kpc to align with a secondary preferred axis. This results in slight differences in the observed inclination and PA curves, which can be seen in the 3D data plane by projecting the results onto several positional velocity slits (as shown in Figure 7).

4.3. Residuals as nonrotating components

In all three models, there exist molecular gas regions that cannot be fitted by circular orbits (deviating by a fiducial velocity of 50 km s^{-1} or more from each best-fitting model) and that are thus considered kinematic outliers. Specifically, models A and B fit 80% of all molecular clouds, while model C fits 94% of them. The residuals correspond to clouds of interest for inflows/outflows, and they are clustered in the four areas (R1, R2, R3, and R4) shown in Figure 7.

Two of these regions are located in the central disk region: a set of CO(3–2) clumps (referred to as **R1**) at the very center (≤ 120 pc) and a CO(2–1) clump located at a projected distance of $R \approx 200$ pc in the NW (PA = -50° to -60°) referred to as **R2**. Both of these regions exhibit deviations of more than 100 km s^{-1} from the circular velocity model (panel C in Figure 8). To explore all possible kinematic scenarios for these regions, we first examine whether they could be intrinsically located at larger radii, with projection properties different from those identified by our code – a scenario that we rule out.

We start with R2, the region that exhibits the highest deviation ($dV \sim -150 \text{ km s}^{-1}$), to investigate whether it could be located at kpc scales. Its maximum projected velocity can be estimated using the equation $V_{\text{los}} = V(r) \frac{\sin i \sin \delta\phi}{\sqrt{1 + \tan^2 i \cos^2 \delta\phi}}$, where $\delta\phi = \phi - \text{PA}$ is the angular distance between the PA of the orbit and the position of the cloud, and $V(r)$ is the intrinsic rotational velocity. By combining this equation with $R(\phi)$, the sky-projected distance of

the orbit with radius r , we can compute the maximum projected velocity as

$$V_{\text{los}}^{\text{max}}(R) = V(r) \frac{R}{r} \cos i \sqrt{\tan^2 i - \left(\frac{r}{R}\right)^2 - 1}. \quad (10)$$

For an intrinsic rotational velocity of 350 km s^{-1} at $r = 650$ pc, the maximum projected velocity would be $\sim 100 \text{ km s}^{-1}$ (panel A in Figure 8). For larger distances, this value would decrease, indicating that there is no possible circular orbit projection that can explain the observed deviation. Therefore, R2 must be located in the inner disk. Furthermore, its projected velocity ($200 - 250 \text{ km s}^{-1}$) is close to the maximum value that the potential can support (and higher than our best-fitting value). This implies that R2 must be close to the PA of a nearly edge-on orbit, which contradicts the evidence that the rest of the gas at similar radii is moving in the reverse direction and with a different orientation (PA = 72°). Therefore, if R2 is not counter-rotating, it must be in an outflow (or an inflow).

Regarding the high-velocity structure R1, similar conclusions can be drawn. High distances are ruled out by Equation 10. Conversely, very small distances (≤ 120 pc from the center) and beam smearing (with a CO(3–2) beam of 95 pc) can potentially raise doubts about its central location. If the gas were regularly rotating and the deviation were induced by a beam smearing effect, then its sky-projected distance from the center must be $R < 50$ pc (panel B of Figure 8). However, at its maximum extent, R1 reaches a distance of $R \approx 120$ pc from the center (panel C of Figure 8), larger than the major axis of the CO(3–2) beam (93 pc). Thus, we can safely conclude that R1 is also a nonrotating clump. In conclusion, the two central components, R1 and R2, are unlikely to be attributed to a regularly rotating disk, but are instead tracing outflowing (or inflowing) gas.

Both components exhibit high-velocity dispersion, implying that the gas is either in a highly turbulent dynamical state or that it experiences a large velocity gradient ($> 200 \text{ km s}^{-1}/100 \text{ pc}$) due to acceleration. Previous observations of NGC6328 also indicate the presence of both inflowing and outflowing gas, based on their relative velocity to the source. In front of the radio source, Maccagni et al. (2018) observed a CO(2-1) clump in absorption, redshifted at $\sim 340 \text{ km s}^{-1}$ and with a velocity dispersion of $\sim 60 \text{ km s}^{-1}$. Absorption features have also been detected in HI (Maccagni et al. 2014). One of them is broad, with a width of 65 km s^{-1} , and it is redshifted to a velocity of 26 km s^{-1} . The second one is narrower, with a width of 43 km s^{-1} , and it is blueshifted to a velocity of -74 km s^{-1} .

Based on the gas kinematic model and the observed dust extinction, we can deduce that the northern side of the inner disk corresponds to its near side (between the center of the galaxy and the observer). Hence, the blueshifted clump is outflowing from the disk. Similarly, the redshifted southern component, R1, on the far side of the inner disk, is also outflowing. This scenario is depicted in Figure 9.

The outflow scenario is also supported by two other arguments. The first is the existence of a broad kinematic component at the same locations in the ionized gas emission, as seen in recent optical, X-shooter data. The spectra, extracted from a slit with PA = 160° , are shown in Figure 10. They illustrate the 5007 Angstrom [OIII] emission at three different positions along this slit: R2, located 219 pc North-East (NE) of the center, the central region at -30 pc, and the southwest region at 160 pc. The spectra at each location are summed over four spectral pixels, and cover a width of > 100 pc. For all regions, the gas exhibits similar narrow ($\sigma = 80 - 180 \text{ km s}^{-1}$) and broad ($\sigma = 460 - 660 \text{ km s}^{-1}$)

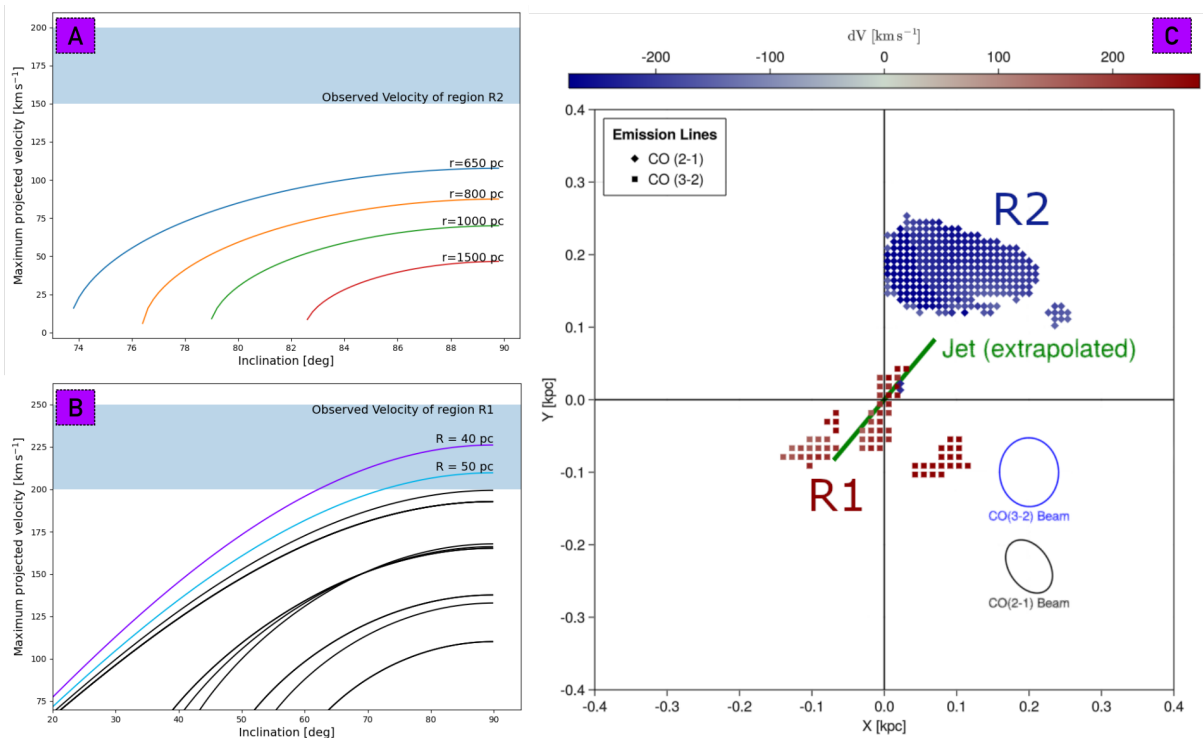


Fig. 8: Residuals in the central disk region. **A**: Maximum projected velocity based on a clump located at a projected radius $R = 200$ pc for different possible orbit radii and inclinations. The blue band represents the observed projected velocity of the CO(2 – 1) emission lines. **B**: Maximum projected velocity based on a clump located in the central $R \approx 50$ pc for different possible orbit radii and inclinations. The blue band represents the observed projected velocity of the CO(3 – 2) emission lines. **C**: Emission line residuals ($\delta V > 100$ km s⁻¹) in the central 500 pc disk area in the sky plane. Circles represent the CO(2 – 1) emission and rectangles CO(3 – 2). The green vector is the extrapolated direction of the jet.

emission line components, and in the last two regions, an extra blueshifted high-velocity component is seen at ≈ 630 km s⁻¹. All these findings constitute direct evidence of the presence of strong winds in the inner disk of NGC6328.

The second argument favoring the existence of an outflow is the CO excitation. From the ratio of CO(3 – 2) and CO(2 – 1) cubes (both re-imaged to a common resolution), we estimated the excitation of the gas. The brightness temperature ratio cube $T_{\text{CO}(3-2)}/T_{\text{CO}(2-1)}$ significantly exceeds the value for optically thick gas in the local thermodynamic equilibrium (LTE):

$$\frac{T_{\text{CO}(3-2)}}{T_{\text{CO}(2-1)}} = \frac{I_{\text{CO}(3-2)}}{I_{\text{CO}(2-1)}} \left(\frac{\nu_{\text{CO}(2-1)}}{\nu_{\text{CO}(3-2)}} \right)^2 \stackrel{\text{LTE}}{=} \frac{9}{4}. \quad (11)$$

We observe significantly higher brightness temperature ratios in (and close to) R1, while the bulk of the regularly rotating molecular gas is sub-thermally excited (Figure 11). The high excitation ratio could be the result of extra density components, of evaporation of the outer cloud layers that makes them optically thin, or of the presence of extra excitation mechanisms (e.g., shocks, cosmic rays) in the outflow. Similar results for the molecular gas excitation have been obtained in the nearby galaxies IC 5063 (Dasyra et al. 2016) and NGC3100 (Ruffa et al. 2022) and demonstrated to have been induced by an interaction between the radio jets and the surrounding cold gas. These results also suggest that the high-velocity clump in R1 corresponds to a co-spatial and also kinematically deviating warm H₂ component (Maccagni et al. 2016b). The other two locations of interest cover part of the high-velocity dispersion regions at kpc distances, to the southwest (**R3**)

and northeast (**R4**) of the center (as previously mentioned in Section 2.1). For these regions, the fraction of fitted clouds shows a significant discrepancy between models A, B (63% fitted), and C (91% fitted) when introducing a $10^\circ - 20^\circ$ wobble in the $\theta(r)$ curve (panel A of Figure 4). This wobble can be caused by more than one asymmetry in the total potential, such as stronger bulge triaxiality, nonspherical dark matter potential, a disk, or a bar. Similar wobbles in the polar angle have been observed at 100 pc scales in M84 (Quillen & Bower 1999), where the authors also suggest the presence of torques caused by the AGN radiation pressure. However, the lack of strong observable asymmetry signatures (e.g., bars) in optical or near infrared images raises the possibility that R3 and R4 are also regions of noncircular motions, and – namely – outflows. In R3, some CO-emitting clouds that are more excited than average are also identified. The ionized gas kinematics there do not show a broad emission component, but different velocities than the disk. Leaving the outflow scenario as an open option there, we proceed to the identification of the driving mechanism of the certainly outflowing gas.

5. Discussion

Our best models describing the evolution of the majority of the gas disk suggest a recent episode (100 – 400 Myrs) of gas accretion. Numerical simulations conducted by van de Voort et al. (2015) predict that a merger can cause such a strong inflow of gas, followed by strong outflows through which the gas can be expelled and re-accreted. These accretion episodes can result in a misalignment between the gas and the galaxy potential, which

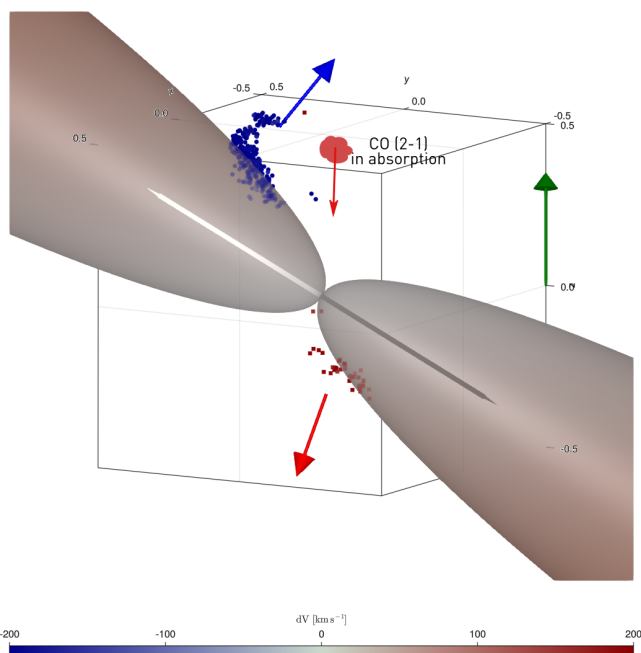


Fig. 9: Emission line residuals ($dV > 100 \text{ km s}^{-1}$) in the central 500 pc disk from another angle. Circles represent the CO(2 – 1) emission and rectangles CO(3 – 2). The conical shapes represent a hypothetical jet-driven bubble responsible for the molecular gas outflow. The green vector shows the direction of the observer. Blue and red vectors show the possible direction of the observed outflows.

under the process of gravitational relaxation forms a warped disk due to the gravitational torques of the stellar potential. This process has been recently observed in NGC5077 (Raimundo 2021) and NGC3100 (Ruffa et al. 2022; Maccagni et al. 2023), where the misaligned cold gas feeds the SMBH and triggers similar outflows.

5.1. What drives the outflow

Energetic and momentum arguments are often used as indicators of the outflow driving mechanism. In order to estimate the mass outflow rate, kinetic power, and momentum, we considered the starting position, velocity, and geometry of the outflow. This is assumed to emanate from a central region and travel outward, so its geometry can be approximated by a cone or sphere. In this context, the term r_{out} refers to the distance the outflow has traveled from its origin, representing a measure of how far the material has been carried by the outflow. This simplifying assumption may not always hold, but it is frequently made in the literature.

The outflow mass rate can then be described by the equation

$$\dot{M}_{\text{out}} = C \frac{M_{\text{out}} V_{\text{out}}}{r_{\text{out}}} \quad (12)$$

where M_{out} and V_{out} represent the mass and velocity of the outflow, respectively, and C is a parameter that depends on the outflow history (Lutz et al. 2020). We use a value of $C = 1$, which assumes that the outflow we are observing now has started at a point in the past and continued with a constant mass outflow rate until now. Another value used in the literature is $C = 3$, which takes into account that the outflowing gas has a constant average volume density in a cone or a sphere. For the outflow

travel distance, we assumed an indicative value of $r_{\text{out}} \approx 100 \text{ pc}$, as this is a typical distance if the outflow has originated locally from a nearby part of the disk (instead of in the center of the galaxy). For the outflowing mass, we used a conversion factor of $a_{\text{CO}} = 0.8 M_{\odot} (\text{K km s}^{-1} \text{ pc}^2)^{-1}$. This value is lower than that typically adopted, as we made the assumption that both R1 and R2 have optically thin parts due to interaction with the AGN or jet (Cicone et al. 2014; Dasyra et al. 2016; Ruffa et al. 2022).

To calculate the outflow velocity, V_{out} , we used the velocity deviating from the best-fitting model. However, this value needs to be corrected for the outflow angle. We tried two different approaches in estimating V_{out} , first by using the estimation of $V_{\text{out}} = |\Delta v| + 0.12 \sigma_v$ proposed by Lutz et al. (2020), where σ_v is the velocity dispersion of each cloudlet (emission line per pixel) in the outflow. Then, we used a projection angle based on a uniform distribution from -30 to 30° from the disk and adopted the mean value. This represents all the possible angles in a cone centered to the disk itself with a maximum opening toward the observer. Both methods provided similar results, which are presented in Table 2 and compared to molecular outflows detected in the literature in Figure 12. In the event that the outflow originated from the center of the galaxy and had a constant average volume density (i.e., $C = 3$), these results would only be a factor of two higher.

Table 2: Molecular outflow properties

Region	Mass	\dot{M}_{out}	Kinetic Power	Momentum Rate
	$10^6 M_{\odot}$	$M_{\odot} \text{ yr}^{-1}$	$10^{40} \text{ erg s}^{-1}$	10^{33} dyn
R1	0.12	0.2	0.3	0.23
R2	1.9	2.9	2.4	2.8
Total	2.02	3.1	2.7	3

We are able to estimate the likelihood of the observed outflow being driven by energy injection from local SF –supernovae (SNae) – or from the AGN. Based on the formula presented in Sullivan et al. (2006), the rate of Type Ia SNae is given by $\Gamma = 5.3 \times 10^{-3} \frac{M}{10^{11} M_{\odot}} + 3.9 \times 10^{-4} \frac{\text{SFR}}{M_{\odot} \text{ yr}^{-1}} \text{ SN yr}^{-1}$. This leads to an estimated power output of

$$\dot{E}_{\text{SN}} = 1.68 \times 10^{41} \frac{M}{10^{11} M_{\odot}} + 1.24 \times 10^{40} \frac{\text{SFR}}{M_{\odot} \text{ yr}^{-1}} \quad (13)$$

Our estimate of the total stellar mass within a radius of 200 pc, as derived from our modeling, is $10^9 M_{\odot}$ (or 0.6% of the total stellar mass). Using this value and assuming that the SF rate (estimated to be $1 - 2 M_{\odot} \text{ yr}^{-1}$, according to Willett et al. 2010) is proportional to the stellar mass distribution, we estimate the SNae’s kinetic power to be $1.8 \times 10^{39} \text{ erg s}^{-1}$. This is an order of magnitude below the lower limit of the outflow total kinetic power. This suggests that the power from SNae alone is not the main driver of the outflow.

On the other hand, for the low-luminosity AGN ($L_{\text{AGN}}/c \approx 4.3 \times 10^{31} \text{ dyn}$), the kinetic energy ratio of $\dot{E}_{\text{out}}/L_{\text{AGN}} \sim 0.02$ is consistent with the scenario of a wind driven by the AGN radiation pressure. However, the momentum rate ratio of $\dot{p}_{\text{out}}/L_{\text{AGN}}/c \sim 60$ is large even for an intermittent AGN episode scenario, as noted in Zubovas & Nardini (2020).

The power of the radio jet in NGC6328 has been estimated to be $2 \times 10^{42} \text{ erg s}^{-1}$ through SED fitting (Sobolewska et al. 2022). However, the use of the calorimetric scaling relation involving the $L_{1.4\text{GHz}}$ luminosity from Willott et al. (1999), Birzan et al. (2008), and Cavagnolo et al. (2010) yields a similar value

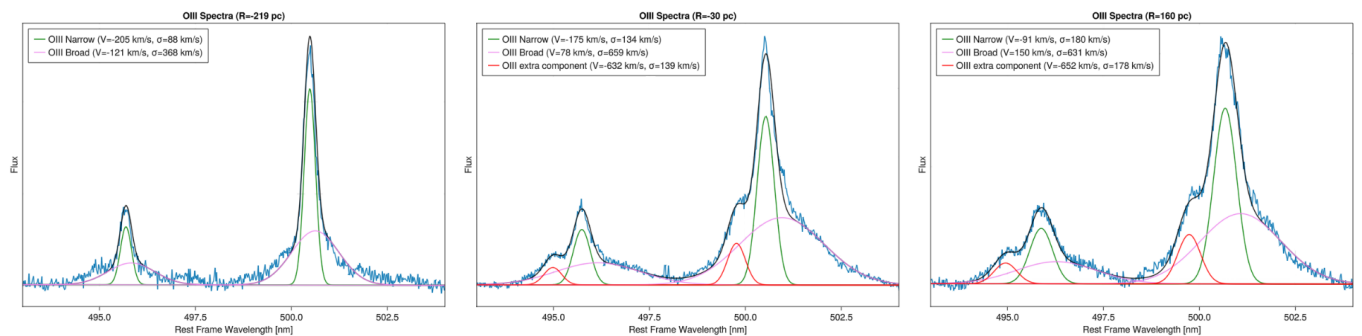


Fig. 10: [OIII] spectrum centered in three different positions along a 240 pc-wide slit (PA 160°). From left to right, -220 pc, -30 pc, and 160 pc from the nucleus. For every position the signal (blue) is averaged out over four pixels, corresponding to a physical width of 142 pc along the slit. In each spectrum, we have fitted one narrow and one broad component. At the -30 pc and 160 pc positions, an additional blueshifted (≈ 600 km s^{-1}) component was required to obtain a good fit.

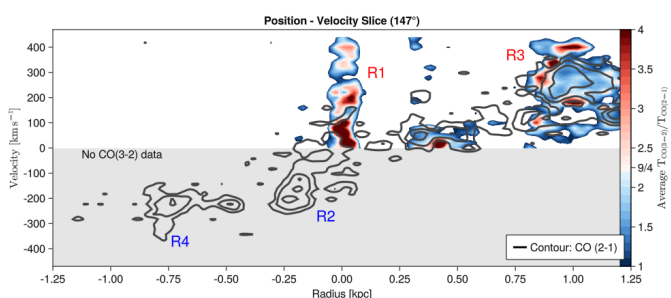


Fig. 11: Position velocity slice along the PA of 147° . The values represent the average value of $T_{CO(2-1)} / T_{CO(3-2)}$ and the contours the CO(2-1) intensity.

of $2 - 3 \times 10^{43}$ erg s^{-1} , which is an order of magnitude higher than the estimate obtained from SED fitting. According to Wójtowicz et al. (2020), the minimum jet power is estimated to be 2.7×10^{42} erg s^{-1} under the assumption of energy equipartition between the magnetic field and radio-emitting electrons within the lobes. Even with this minimum estimate, it is still clear that the jet has more than enough energy to drive the outflow and play a significant role in boosting or supporting the AGN's overall impact on its surroundings. Numerical hydrodynamic simulations by Mukherjee et al. (2016) have shown that low-powered jets can have a greater impact on the ISM due to their prolonged interaction and difficulty in escaping into intergalactic space.

5.2. Why can we not see the jet?

The fact that the outflow observed in NGC6328 is further away from the nucleus than the currently detected radio emission is consistent with other sources where molecular winds trace previously undetected radio jets, as seen in cases such as NGC1377 (Aalto et al. 2016), 4C31.04 (Zovaro et al. 2019), and ESO420-G13 (Fernández-Ontiveros et al. 2020).

One potential explanation for the lack of radio emission in NGC6328 could be due to recurrent jet-launching powered by stochastic feeding. In this scenario, the energy from previous jets may have been deposited onto large bubbles of kpc scales a long time ago, leading to the cooling of cosmic rays in these bubbles, and thus to the lack of detected radio emission. Using the same assumptions of the outflow properties, it is estimated

that the outflow originated $t_{out} = 200 - 700$ kyrs ago (depending on the possible values of r_{out}). The magnetic field at pc scales is estimated to be $B \approx 10^{-2}$ G (Tingay et al. 1997), and the synchrotron cooling time at 0.1 kpc scales is computed to be $t_{cool,syn} \approx 150$ kyrs. This cooling time could be significantly reduced if inverse Compton (IC) cooling were taken into account or if the magnetic field during the previous cycle of the jet were significantly higher. By comparing these two timescales, it can be argued that a highly magnetized relic of a turned-off jet can fade away within an AGN duty cycle due to synchrotron cooling, shock-induced cooling, and adiabatic losses. Such a jet would have been capable of providing mechanical and radiative feedback to the intergalactic medium up to kpc scales. In the case of a mass-loaded jet, in which hadronic radiative processes are important (Reynoso et al. 2011; Rieger 2017), cavities will be observed in cold molecular gas due to photo-dissociation by X-ray and gamma-ray photon fields emanating from the jets (Maloney et al. 1996; Wolfire et al. 2022).

Another scenario that could explain the lack of radio emission in NGC6328 is the relativistic de-boosting. This occurs when the radio emission from the jet is directed away from the observer, reducing its apparent luminosity and making it more challenging to detect. To assess the impact of relativistic de-boosting, we used radio imaging and the velocity of the radio blobs, as determined through VLBI (estimated to $\beta_{app} = 0.13 \pm 0.06$ from Angioni et al. 2019), to calculate the jet/counter-jet flux density ratio, which we estimated to be $R = 1.4 \pm 0.1$ at 8.4 GHz. The intrinsic β and jet inclination, θ_{jet} can be estimated by solving the set of equations,

$$\beta_{app} = \frac{\beta \sin \theta}{1 - \beta \cos \theta} \quad R = \left(\frac{1 + \beta \cos \theta}{1 - \beta \cos \theta} \right)^{p-\alpha} \quad (14)$$

where $\alpha = -1.5$ is the spectral index and p is a parameter that takes the values two or three depending on whether R is calculated from an integrated flux across a continuous jet or a single component (Angioni et al. 2019). Assuming $p = 3$ for a single moving component that dominates the 8.4 GHz core radio flux, we estimated $\beta = 0.14 \pm 0.05$ and $\theta_{jet} = 68^\circ \pm 17^\circ$. These results are robust with regard to variations in the p parameter; using $p = 2$ yields similar values within the error margins, with θ having a central value of 62° . Based on these parameters, the Lorentz factor, Γ , is approximately 1.02 , and the corresponding relativistic boost factor $\delta \sim 1.02$. Given the modest value of δ , it is unlikely that relativistic de-boosting is responsible for obscuring the jet from detection.

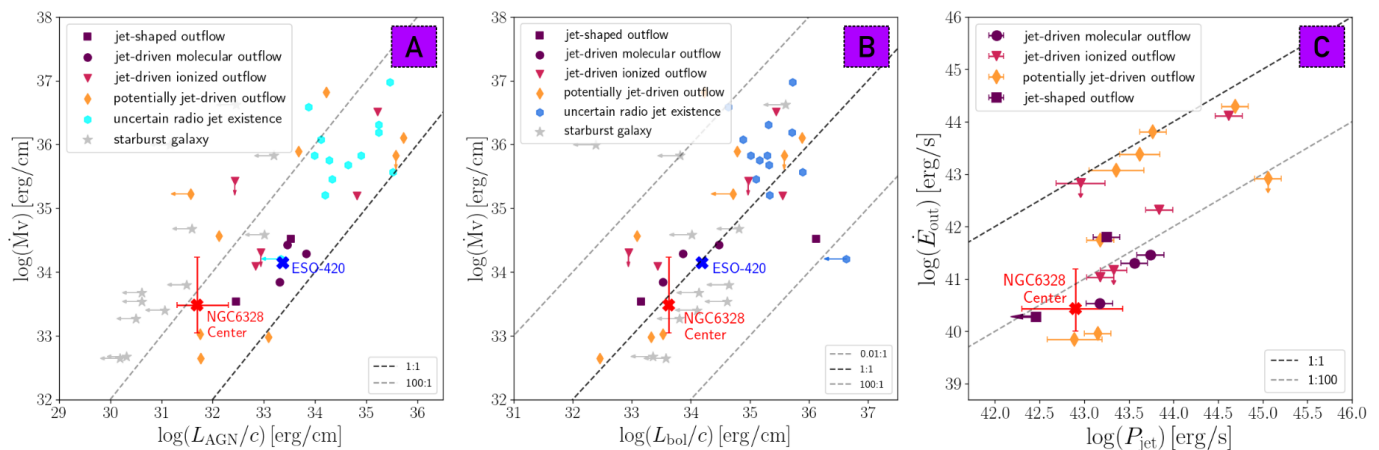


Fig. 12: Wind vs. driving mechanism energetics for local galaxies with massive molecular wind detections. **A:** Wind momentum rate vs. radiation pressure of AGN photons. **B:** Wind kinetic luminosity vs. jet power. The dashed lines indicate different ratios of the plotted parameters. **C:** Outflow’s momentum rate relation with the total photon momentum output of the galaxy. The dashed lines denote the different values of the ratio of outflow’s momentum rate over bolometric luminosity. The arrows denote upper limit values.

However, jet acceleration and collimation in AGN have been observed to occur over distances of $10^4 - 10^6 R_s$ (Blandford et al. 2019; Kovalev et al. 2020; Okino et al. 2022; Baczko et al. 2022; Roychowdhury et al. 2023), which corresponds to more than 0.5 kpc for a black hole with a mass of $4 \times 10^8 M_\odot$. This length scale is similar to the size of the radio structure (~ 1 kpc) observed by VLBI in the present case. Assuming an inclination angle of $\approx 65^\circ$ suggests that under sufficient acceleration ($\Gamma > 5$ a typical value for relativistic jets) the jet could reach a de-boosting factor of $\delta^4 \gtrsim 0.01$, making it too faint to be detected by radio telescopes. Additionally, the decrease in magnetic field strength (roughly r^{-1} for a collimated jet; Vlahakis & Königl 2004; Fendt 2006; Porth et al. 2011) could further reduce the radio luminosity and explain the lack of radio flux beyond 100 kpc. At the same time, efficient IC cooling due to an abundance of ambient photons could explain the extended X-ray (Beuchert et al. 2018) and gamma-ray (Migliori et al. 2016) components observed in the source spectrum, and the suppression of any extended radio emission by insufficient synchrotron cooling. The presence of a hidden, extended jet would offer greater kinetic power than the current estimations through SED fitting ($\approx 10^{43}$ erg s $^{-1}$), and could transfer energy over kpc scales, possibly contributing to the observed excited warm H $_2$ (Maccagni et al. 2016b) and extended soft X-ray component (Beuchert et al. 2018).

5.3. The jet-outflow connection in nearby galaxies with massive outflows of cold molecular gas

Motivated by the possibility of a jet-ISM interaction in NGC6328, we evaluate whether the role of jets as drivers of gas outflows has been underestimated due to the criterion typically employed for this evaluation. The evaluation primarily involves a parameter, q_{ir} (Iverson et al. 2010), defined as the logarithmic ratio of the observed far-infrared flux to the 1.4 GHz radio flux. In starburst galaxies, these two quantities correlate due to the synchrotron and dust emission around SNaE (Helou et al. 1985). Consequently, q_{ir} falling below a critical value (indicating radio excess) has been interpreted as a criterion of radio loudness (Iverson et al. 2010). In a recent compilation of 45 local galaxies with massive molecular outflows, most galaxies were not radio loud based on

this criterion and, consequently, jets were deemed to be a rare outflow-launching mechanism (Fluetsch et al. 2019).

However, the discovery of galaxies with jet-shaped outflows but without (strong) associated radio emission (Aalto et al. 2020; Fernández-Ontiveros et al. 2020) demonstrates that the radio excess is an unsafe criterion. Outflows can remain once the jets that initiated them fade or move away. We thus reevaluated the jet-outflow connection in these sources, primarily by spatial distribution criteria and secondarily by energetic criteria (see Appendix 5.3). We find that a plausible jet-outflow connection exists in about half of the examined AGN, as the jet coincides with or extends in the same direction as the outflow. This is true for almost all AGN of low luminosity ($\lesssim 10^{11} L_\odot$). From an energetic viewpoint, the jet can sustain the outflow in nearly all spatially identified cases, as the jet power (cavity and synchrotron included) exceeds the outflow kinetic energy. The impact of jets on the molecular ISM could therefore concern a high fraction of local AGN with massive outflows.

6. Conclusions

We present a novel tilted-ring code capable of fitting ALMA cubes in a Bayesian framework, by inferring the intrinsic 3D distribution of the gas. The code incorporates a differential precession model in a triaxial axisymmetric potential (e.g., that of a nonspherical Hernquist bulge), and additionally offers a model that treats rings as independent entities, with interpolation between them to derive their geometrical properties. When applied to CO(2–1) and CO(3–2) ALMA data of the central 4 kpc of NGC6328, it indicated that the cold gas has settled into a stable inner disk in the central 600 pc 100–400 Myrs on from its initial configuration. The orientation of the disk rapidly changes over the next 1–2 kpc, explaining the observable high dispersion regions in these areas. We also detect the presence of outflowing molecular gas in at least two (and up to four) regions in the central 200 pc of the galaxy. From an energetic viewpoint, the jet is the most plausible mechanism that can sustain the outflow, adding NGC6328 to the catalog of jet-ISM interacting sources where the jet is not detected in the outflow region. We have discussed two possible mechanisms of how this can happen, due to either recur-

rent jet-launching powered by stochastic feeding or relativistic de-boosting of the jet brightness in the event that the jet becomes collimated after the 2 pc that is currently visible.

Acknowledgements. This project has received funding from the Hellenic Foundation for Research and Innovation (HFRI) and the General Secretariat for Research and Technology (GSRT), under grant agreement No 1882. JAO acknowledges financial support by the Spanish Ministry of Science and Innovation (MCIN/AEI/10.13039/501100011033) and “ERDF A way of making Europe” through the grant PID2021-124918NB-C44; MCIN and the European Union – NextGenerationEU through the Recovery and Resilience Facility project ICTS-MRR-2021-03-CEFCA. IR acknowledges support from grant ST/S00033X/1 through the UK Science and Technology Facilities Council (STFC). The figures of this paper have been created through Julia Packages of Makie.jl (Danisch & Krumbiegel 2021) and Python’s Matplotlib (Hunter 2007). Corner Plots are created with PairPlots.jl (Thomson 2022) This paper makes use of the following ALMA data: ADS/JAO.ALMA#2015.1.01359.S, and ADS/JAO.ALMA#2017.1.01638.S. ALMA is a partnership of ESO (representing its member states), NSF (USA) and NINS (Japan), together with NRC(Canada) and NSC and ASIAA (Taiwan), in cooperation with the Republic of Chile. The Joint ALMA Observatory is operated by ESO, AUI/NRAO and NAOJ. The National Radio Astronomy Observatory is a facility of the National Science Foundation operated under cooperative agreement by Associated Universities, Inc.

References

- Aalto, S., Costagliola, F., Muller, S., et al. 2016, *Astronomy & Astrophysics*, 590, A73
- Aalto, S., Falstad, N., Muller, S., et al. 2020, *Astronomy & Astrophysics*, 640, A104
- Alatalo, K., Blitz, L., Young, L. M., et al. 2011, *The Astrophysical Journal*, 735, 88
- Allison, J. R., Sadler, E. M., & Meekin, A. M. 2014, *Monthly Notices of the Royal Astronomical Society*, 440, 696
- Alonso-Herrero, A., Pereira-Santaella, M., García-Burillo, S., et al. 2018, *The Astrophysical Journal*, 859, 144
- Angioni, R., Ros, E., Kadler, M., et al. 2019, *Astronomy & Astrophysics*, 627, A148
- Antonucci, R. 1993, *Annual Rev. Astron. Astrophys.*, Vol. 31, p. 473-521 (1993), 31, 473
- Audibert, A., Combes, F., García-Burillo, S., et al. 2019, *Astronomy & Astrophysics*, 632, A33
- Audibert, A., Dasyra, K. M., Papachristou, M., et al. 2022, *A&A*, 668, A67
- Baan, W. A. & Klöckner, H.-R. 2006, *Astronomy & Astrophysics*, Volume 449, Issue 2, April II 2006, pp.559-568, 449, 559
- Baczko, A.-K., Ros, E., Kadler, M., et al. 2022, *Astronomy & Astrophysics*, 658, A119
- Baldi, R. D., Williams, D. R. A., McHardy, I. M., et al. 2018, *MNRAS*, 476, 3478
- Baldi, R. D., Williams, D. R. A., McHardy, I. M., et al. 2021, *MNRAS*, 500, 4749
- Beuchert, T., Rodríguez-Ardila, A., Moss, V. A., et al. 2018, *Astronomy & Astrophysics*, 612, L4
- Bezanson, J., Edelman, A., Karpinski, S., & Shah, V. B. 2015, arXiv:1411.1607 [cs] [arXiv:1411.1607]
- Bicknell, G. V., Dopita, M. A., & O’Dea, C. P. O. 1997, *The Astrophysical Journal*, 485, 112
- Bicknell, G. V., Mukherjee, D., Wagner, A. Y., Sutherland, R. S., & Nesvadba, N. P. H. 2018, *Monthly Notices of the Royal Astronomical Society*, 475, 3493
- Binney, J. & Tremaine, S. 2008, *Galactic Dynamics: Second Edition*
- Birzan, L., McNamara, B. R., Nulsen, P. E. J., Carilli, C. L., & Wise, M. W. 2008, *The Astrophysical Journal*, 686, 859
- Blandford, R., Meier, D., & Readhead, A. 2019, *ARA&A*, 57, 467
- Bolatto, A. D., Wolfire, M., & Leroy, A. K. 2013, *Annu. Rev. Astron. Astrophys.*, 51, 207
- Bullock, J. S., Kolatt, T. S., Sigad, Y., et al. 2001, *Monthly Notices of the Royal Astronomical Society*, 321, 559
- Cavagnolo, K. W., McNamara, B. R., Nulsen, P. E. J., et al. 2010, *ApJ*, 720, 1066
- Chandrasekhar, S. 1969, *Ellipsoidal Figures of Equilibrium*
- Cicone, C., Maiolino, R., Sturm, E., et al. 2014, *Astronomy & Astrophysics*, 562, A21
- Clemens, M. S., Scaife, A., Vega, O., & Bressan, A. 2010, *Monthly Notices of the Royal Astronomical Society*, 405, 887
- Clemens, M. S., Vega, O., Bressan, A., et al. 2008, *Astronomy & Astrophysics*, Volume 477, Issue 1, January I 2008, pp.95-104, 477, 95
- Combes, F., García-Burillo, S., Casasola, V., et al. 2013, *Astronomy & Astrophysics*, 558, A124
- Condon, J. J., Cotton, W. D., Greisen, E. W., et al. 1998, *The Astronomical Journal*, 115, 1693
- Condon, J. J., Helou, G., Sanders, D. B., & Soifer, B. T. 1996, *The Astrophysical Journal Supplement Series*, 103, 81
- Cresci, G., Marconi, A., Zibetti, S., et al. 2015, *Astronomy & Astrophysics*, 582, A63
- Croton, D. J., Springel, V., White, S. D. M., et al. 2006, *Monthly Notices of the Royal Astronomical Society*, 365, 11
- Danisch, S. & Krumbiegel, J. 2021, *Journal of Open Source Software*, 6, 3349
- Dasyra, K. M., Bostrom, A. C., Combes, F., & Vlahakis, N. 2015, *The Astrophysical Journal*, 815, 34
- Dasyra, K. M., Combes, F., Oosterloo, T., et al. 2016, *Astronomy & Astrophysics*, 595, L7
- Davies, R. L., Groves, B., Kewley, L. J., et al. 2017, *Monthly Notices of the Royal Astronomical Society*, 470, 4974
- Davis, T. A. & Bureau, M. 2016, *Monthly Notices of the Royal Astronomical Society*, 457, 272
- Davis, T. A., Krajnović, D., McDermid, R. M., et al. 2012, *Monthly Notices of the Royal Astronomical Society*, 426, 1574
- Drake, C. L., Bicknell, G. V., McGregor, P. J., & Dopita, M. A. 2004, *The Astronomical Journal*, 128, 969
- Dumas, G., Schinnerer, E., Tabatabaei, F. S., et al. 2011, *The Astronomical Journal*, 141, 41
- Fabian, A. C. 2012, *Annu. Rev. Astron. Astrophys.*, 50, 455
- Fendt, C. 2006, *The Astrophysical Journal*, 651, 272
- Fernández-Ontiveros, J., Dasyra, K., Hatziminaoglou, E., et al. 2020, *Astronomy & Astrophysics*, 633, A127
- Fluetsch, A., Maiolino, R., Carniani, S., et al. 2019, *Monthly Notices of the Royal Astronomical Society*, 483, 4586
- Fotopoulou, C. M., Dasyra, K. M., Combes, F., Salomé, P., & Papachristou, M. 2019, *Astronomy & Astrophysics*, 629, A30
- Fu, H. & Stockton, A. 2009, *The Astrophysical Journal*, 690, 953
- García-Burillo, S., Combes, F., Almeida, C. R., et al. 2019, *Astronomy & Astrophysics*, 632, A61
- González-Alfonso, E., Fischer, J., Spoon, H. W. W., et al. 2017, *The Astrophysical Journal*, 836, 11
- Greene, J. E., Zakamska, N. L., & Smith, P. S. 2012, *The Astrophysical Journal*, 746, 86
- Grupponi, C., Berta, S., Spinoglio, L., et al. 2016, *Monthly Notices of the Royal Astronomical Society*, 458, 4297
- Harnett, J. I. 1987, *Monthly Notices of the Royal Astronomical Society*, 227, 887
- Harrison, C. M., Costa, T., Tadhunter, C. N., et al. 2018, *Nature Astronomy*, 2, 198
- Helou, G., Soifer, B. T., & Rowan-Robinson, M. 1985, *The Astrophysical Journal*, 298, L7
- Hernquist, L. 1990, *ApJ*, 356, 359
- Hunter, J. D. 2007, *Computing in Science & Engineering*, 9, 90
- Husemann, B., Bennert, V. N., Jahnke, K., et al. 2019a, *The Astrophysical Journal*, 879, 75
- Husemann, B., Scharwächter, J., Davis, T., et al. 2019b, *Astronomy & Astrophysics*, 627, A53
- Iverson, R., Magnelli, B., Ibar, E., et al. 2010, *Astronomy & Astrophysics*, 518, L31
- Johnson, S. G. 2013, *QuadGK.jl: Gauss-Kronrod integration in Julia*, <https://github.com/JuliaMath/QuadGK.jl>
- Kellermann, K. I. & Pauliny-Toth, I. I. K. 1969, *ApJ*, 155, L71
- Kovalev, Y. Y., Pushkarev, A. B., Nokhrina, E. E., et al. 2020, *MNRAS*, 495, 3576
- Krumholz, M. R., McKee, C. F., & Tumlinson, J. 2009, *The Astrophysical Journal*, 699, 850
- Lake, G. & Norman, C. 1983, *ApJ*, 270, 51
- Lanz, L., Ogle, P. M., Alatalo, K., & Appleton, P. N. 2016, *The Astrophysical Journal*, 826, 29
- Leon, S., Eckart, A., Laine, S., et al. 2007, *Astronomy & Astrophysics*, Volume 473, Issue 3, October III 2007, pp.747-759, 473, 747
- Lira, P., Ward, M., Zezas, A., Alonso-Herrero, A., & Ueno, S. 2002, *Monthly Notices of the Royal Astronomical Society*, 330, 259
- Lutz, D., Sturm, E., Janssen, A., et al. 2020, *Astronomy & Astrophysics*, 633, A134
- Maccagni, F. M., Morganti, R., Oosterloo, T. A., & Mahony, E. K. 2014, *Astronomy & Astrophysics*, 571, A67
- Maccagni, F. M., Morganti, R., Oosterloo, T. A., Oonk, J. B. R., & Emonts, B. H. C. 2018, *Astronomy & Astrophysics*, 614, A42
- Maccagni, F. M., Ruffa, I., Loni, A., et al. 2023, *A&A*, 675, A59
- Maccagni, F. M., Santoro, F., Morganti, R., et al. 2016a, *Astron. Nachr.*, 337, 154
- Maccagni, F. M., Santoro, F., Morganti, R., et al. 2016b, *Astronomy & Astrophysics*, 588, A46

- Maloney, P. R., Hollenbach, D. J., & Tielens, A. G. G. M. 1996, *The Astrophysical Journal*, 466, 561
- Marvil, J., Owen, F., & Eilek, J. 2015, *The Astronomical Journal*, 149, 32
- Matsushita, S., Trung, D.-V., Boone, F., et al. 2015, *The Astrophysical Journal*, 799, 26
- McDonald, B., Beaumont, C., Robitaille, T., Ginsburg, A., & E., R. 2013, *astro-dendro*, *Astronomical Dendrograms in Python*, <https://github.com/dendrograms/astrodendro>
- McMullin, J. P., Waters, B., Schiebel, D., Young, W., & Golap, K. 2007, 4
- McNamara, B. R. & Nulsen, P. E. J. 2012, *New Journal of Physics*, 14, 055023
- Migliori, G., Siemiginowska, A., Sobolewska, M., et al. 2016, *ApJ*, 821, L31
- Morganti, R., Oosterloo, T. A., Tadhunter, C. N., et al. 2004, *Astronomy & Astrophysics*, v.424, p.119-124 (2004), 424, 119
- Mukherjee, D., Bicknell, G. V., Sutherland, R., & Wagner, A. 2016, *Monthly Notices of the Royal Astronomical Society*, 461, 967
- Mukherjee, D., Wagner, A. Y., Bicknell, G. V., et al. 2018, *Monthly Notices of the Royal Astronomical Society*, 476, 80
- Navarro, J. F., Frenk, C. S., & White, S. D. M. 1996, *The Astrophysical Journal*, 462, 563
- Neff, S. G., Ulvestad, J. S., & Champion, S. D. 2003, *The Astrophysical Journal*, 599, 1043
- O'Dea, C. P. & Saikia, D. J. 2021, *Astron Astrophys Rev*, 29, 3
- Ohyama, Y., Terashima, Y., & Sakamoto, K. 2015, *The Astrophysical Journal*, 805, 162
- Okino, H., Akiyama, K., Asada, K., et al. 2022, *ApJ*, 940, 65
- Oosterloo, T., Morganti, R., Tadhunter, C., et al. 2019, *Astronomy & Astrophysics*, 632, A66
- Porth, O., Fendt, C., Meliani, Z., & Vaidya, B. 2011, *The Astrophysical Journal*, 737, 42
- Punsly, B. & Kharb, P. 2016, *The Astrophysical Journal*, 833, 57
- Querejeta, M., Schinnerer, E., García-Burillo, S., et al. 2016, *Astronomy & Astrophysics*, 593, A118
- Quillen, A. C. & Bower, G. A. 1999, *ApJ*, 522, 718
- Rackauckas, C. & Nie, Q. 2017, *The Journal of Open Research Software*, 5, exported from <https://app.dimensions.ai> on 2019/05/05
- Raimundo, S. I. 2021, *Astronomy & Astrophysics*, 650, A34
- Revels, J., Lubin, M., & Papamarkou, T. 2016, [arXiv:1607.07892 \[cs.MS\]](https://arxiv.org/abs/1607.07892)
- Reynosó, M., Medina, M., & Romero, G. 2011, *Astronomy & Astrophysics*, 531, A30
- Rieger, F. M. 2017, 1792, 020008
- Roychowdhury, A., Meyer, E. T., Georganopoulos, M., & Kollmann, K. 2023, *arXiv e-prints*, [arXiv:2308.00842](https://arxiv.org/abs/2308.00842)
- Ruffa, I., Davis, T. A., Prandoni, I., et al. 2019, *Monthly Notices of the Royal Astronomical Society*, stz2368
- Ruffa, I., Prandoni, I., Davis, T. A., et al. 2022, *Monthly Notices of the Royal Astronomical Society*, 510, 4485
- Ruffa, I., Prandoni, I., Laing, R. A., et al. 2019, *MNRAS*, 484, 4239
- Ryder, S. D., Buta, R. J., Toledo, H., et al. 1996, *The Astrophysical Journal*, 460, 665
- Sakamoto, K., Aalto, S., Combes, F., Evans, A., & Peck, A. 2014, *The Astrophysical Journal*, 797, 90
- Shimizu, T. T., Mushotzky, R. F., Meléndez, M., et al. 2017, *Monthly Notices of the Royal Astronomical Society*, 466, 3161
- Sijacki, D., Springel, V., Di Matteo, T., & Hernquist, L. 2007, *Monthly Notices of the Royal Astronomical Society*, 380, 877
- Sobolewska, M., Migliori, G., Ostorero, L., et al. 2022, *ApJ*, 941, 52
- Solomon, P. & Vanden Bout, P. 2005, *Annual Review of Astronomy & Astrophysics*, 43, 677
- Solomon, P. M., Downes, D., Radford, S. J. E., & Barrett, J. W. 1997, *ApJ*, 478, 144
- Sparke, L. S. 1996, *The Astrophysical Journal*, 473, 810
- Steiman-Cameron, T. Y. & Durisen, R. H. 1988, *The Astrophysical Journal*, 325, 26
- Sullivan, M., Le Borgne, D., Pritchet, C. J., et al. 2006, *ApJ*, 648, 868
- Talbot, R. Y., Sijacki, D., & Bourne, M. A. 2022, *MNRAS*, 514, 4535
- Teodoro, E. D. & Fraternali, F. 2015, *Monthly Notices of the Royal Astronomical Society*, 451, 3021
- Thomson, W. 2022, *PairPlots.jl* Beautiful and flexible visualizations of high dimensional data. <https://github.com/sefffal/PairPlots.jl>
- Tingay, S. J. & de Kool, M. 2003, *Publ. & #x0096; Astron. Soc. Aust.*, 20, 140
- Tingay, S. J., Jauncey, D. L., Reynolds, J. E., et al. 1997, *The Astronomical Journal*, 113, 2025
- Tingay, S. J., Macquart, J.-P., Collier, J. D., et al. 2015, *AJ*, 149, 74
- Tohline, J. E., Simonson, G. F., & Caldwell, N. 1982, *ApJ*, 252, 92
- Urquhart, R., Soria, R., Johnston, H. M., et al. 2018, *Monthly Notices of the Royal Astronomical Society*, 475, 3561
- Urrutia, T., Becker, R. H., White, R. L., et al. 2009, *The Astrophysical Journal*, 698, 1095
- van de Voort, F., Davis, T. A., Kereš, D., et al. 2015, *Monthly Notices of the Royal Astronomical Society*, 451, 3269
- Varenus, E., Conway, J., Marti-Vidal, I., et al. 2014, *Astronomy & Astrophysics*, 566, A15
- Veilleux, S., Meléndez, M., Sturm, E., et al. 2013, *The Astrophysical Journal*, 776, 27
- Veron-Cetty, M.-P., Woltjer, L., Ekers, R. D., & Staveley-Smith, L. 1995, *Astronomy & Astrophysics*, 297, L79
- Vesselinov, V. V. & O'Malley, D. 2013, *AffineInvariantMCMC.jl*, <https://github.com/madsjulia/AffineInvariantMCMC.jl>
- Vlahakis, N. & Königl, A. 2004, *The Astrophysical Journal*, 605, 656
- Wagner, A. Y. & Bicknell, G. V. 2011, *ApJ*, 728, 29
- Wagner, A. Y., Bicknell, G. V., & Umemura, M. 2012, *ApJ*, 757, 136
- Willett, K. W., Stocke, J. T., Darling, J., & Perlman, E. S. 2010, *ApJ*, 713, 1393
- Willott, C. J., Rawlings, S., Blundell, K. M., & Lacy, M. 1999, *Monthly Notices of the Royal Astronomical Society*, 309, 1017
- Wójtowicz, A., Stawarz, Ł., Cheung, C. C., et al. 2020, *ApJ*, 892, 116
- Wolfire, M. G., Vallini, L., & Chevance, M. 2022, *Annual Review of Astronomy & Astrophysics*, Volume 60, pp. 247-318, 60, 247
- Zovaro, H. R. M., Sharp, R., Nesvadba, N. P. H., et al. 2019, *Monthly Notices of the Royal Astronomical Society*, 484, 3393
- Zschaechner, L. K., Walter, F., Bolatto, A., et al. 2016, *The Astrophysical Journal*, 832, 142
- Zubovas, K. & King, A. 2012, *ApJ*, 745, L34
- Zubovas, K. & Nardini, E. 2020, *Monthly Notices of the Royal Astronomical Society*, 498, 3633

Appendix A: Clump detection

We implemented a source detection process that encodes the data cube into a set of M , individual clumps with sky projected coordinates $\{(x_m, y_m, V_m)\}_{m=1}^M$, through a source detection process. The first step in the process was iterating over all the spaxels of the cube and fitting N Gaussian-shaped emission lines per spaxel (x, y) using the equation

$$S^{x,y}(V, \{V_c\}_{i=1}^N, \{F_i\}_{i=1}^N, \{\sigma_i\}_{i=1}^N) = \sum_{i=1}^N F_i \exp\left(-\frac{(V - V_{c_i})^2}{2\sigma_i^2}\right)$$

The number of Gaussian components, N , was determined by using the Bayesian information criterion (BIC) as a model comparison criterion that balances the goodness of fit and the number of model parameters. Assuming that the likelihood of observing the signal on each spaxel is a Gaussian with a root mean square noise, σ_F , the BIC was defined as

$$\text{BIC} = \chi^2 + k \log(n) + n \log(2\pi \sigma_F^2)$$

where k is the number of fitted parameters, which in our case is $k = 3 \times N$, and n the size of the signal in one spaxel. Adding more Gaussian components to the emission line model can lead to overfitting of the data, whereby the model becomes too complex and captures the noise. To prevent overfitting, we stopped adding more components to the model when the BIC was minimized.

After the process of fitting multiple lines-sources per spaxel was finished, we merged them together into single clumps by starting from the brightest source and following the dropping flux to their neighbors. This methodology is similar to the astronomical dendrograms algorithm that we also tested by using the astrodendro package in Python (McDonald et al. 2013).

The reason we introduced our new methodology rather than directly using the similar estimated clumps from astrodendro is that we wanted to use physically motivated constraints to the fitting procedure. For example, the dendrogram algorithm can combine fluxes to the same clump ("leaf") with a final velocity dispersion of $\sim 80 \text{ km s}^{-1}$ or with sizes of a few kpc as the data is smooth enough to support it. As our intention was to fit a warped disk, assuming typical molecular clumps properties, we added constraints supporting our scenario. However, the comparison of the two methods gives similar results.

Appendix B: Transformation of sky coordinates

In order to transform the positions of gas clouds from galactic to observed sky coordinates, a transformation matrix was needed. This matrix was constructed by using a known vector in the galactic coordinates, \hat{N}_g , and its counterpart, which serves as a reference ring in the sky coordinates, \hat{N}_s :

$$\mathbf{R} = \mathbf{I} + \mathbf{U} + \frac{\mathbf{U} \cdot \mathbf{U}}{1 + \hat{N}_g \cdot \hat{N}_s} \quad (\text{B.1})$$

where \mathbf{U} is the skew-symmetric cross-product matrix of $u = \hat{N}_g \times \hat{N}_s$,

$$\mathbf{U} = \begin{bmatrix} 0 & -u_3 & u_2 \\ u_3 & 0 & -u_1 \\ -u_2 & u_1 & 0 \end{bmatrix} \quad (\text{B.2})$$

As the disk settles toward the preferred axes of the stellar potential, we selected the reference ring to mirror these axes,

thereby setting $\hat{N}_g = \hat{z}$ (in the galaxy coordinates). The same vector in the sky coordinates corresponds to the vector defined by two angles, i_{Bulge} and PA_{Bulge} , as given by

$$\hat{N}_s = \begin{pmatrix} \sin i_{\text{Bulge}} \cos \text{PA}_{\text{Bulge}} \\ \sin i_{\text{Bulge}} \sin \text{PA}_{\text{Bulge}} \\ \cos i_{\text{Bulge}} \end{pmatrix} \quad (\text{B.3})$$

Appendix C: Literature review

To evaluate the fraction of galaxies that our results concern, we gathered literature-based evidence for links between jets and local galactic outflows. For this purpose, we used a recent compilation of local galaxies with molecular outflows (Fluetsch et al. 2019), which we expanded with four more galaxies that had a molecular outflow detection (NGC6328, NGC1377, NGC3100, and ESO420-613). Instead of the radio excess as a criterion for the examination of the jet-outflow connection, we used the following classification scheme for the AGN in the sample: 1) sources with a jet that accelerates molecular gas along its trajectory, 2) sources with a jet that accelerates atomic gas along its trajectory and that can then entrain molecular gas in a multiphase wind model (Zubovas & King 2012), 3) sources with a jet that could be related to the gas acceleration, as it spatially coincides with or extends in a similar direction to the outflow.

The first group of sources comprises IC5063, M51, and NGC1068. In these galaxies, the jet is associated with part of the molecular gas acceleration, with accelerated blobs and outflow starting points along the jet path. IC5063, which has at least four outflow starting points besides the nucleus, is the prototype of this category (Dasyra et al. 2015). In the Seyfert 2 galaxy M51, outflowing molecular blobs are detected near the radio jet outline and the gas excitation changes as a function of distance from the jet (Querejeta et al. 2016; Matsushita et al. 2015). In NGC1068, molecular gas is being entrained at known regions of jet-cloud interaction along the spatially resolved radio jet. This jet-launched outflow adds to the mass of a wind launched by the AGN accretion disk (García-Burillo et al. 2019). NGC1377 and ESO420-613 also belong to this category, with a jet-shaped outflow that probes the synchrotron emission. The radio-quiet galaxy NGC1377 hosts a molecular outflow that is spatially resolved and jet-shaped, with a width of only $\sim 5 - 20 \text{ pc}$ along a length of 150 pc . The outflow revealed the existence of a radio jet that remained elusive in radio images (Aalto et al. 2020). In the Seyfert 2 galaxy ESO420-613, ALMA CO data of 30 pc resolution reveals the existence of a massive outflow far from the nucleus and along the minor axis with a jet-trailing shape: filamentary emission precedes bifurcated emission at a presumed jet-ISM impact point (Fernández-Ontiveros et al. 2020), as in IC5063. Weak radio emission encompasses the outflow location, but its intrinsic shape is unknown as the resolution of the data is considerably lower than that of ALMA.

In the second group, the jet has been proven to accelerate atomic gas, with wind starting points along its path. A molecular outflow also exists in these sources, but its connection with the jet remains to be proven. Still, in the current view of multiphase outflows, the passage of an ionized wind by molecular clouds initiates a molecular outflow, as ram pressure and hydrodynamic instabilities peel off the outer cloud layers. Any wind is thus likely to have both atomic and molecular content. A prototype for this category is Mrk1014, in which an ionized oxygen wind, seen in [OIII], exists at a radio hot spot $\sim 3 \text{ kpc}$ away from the nucleus (Fu & Stockton 2009). An OH outflow, unresolved at

these scales, also exists at the nucleus (Veilleux et al. 2013). In 4c12.50, atomic hydrogen is seen in absorption in front of the radio-jet tip (Morganti et al. 2004). A nuclear, high-velocity CO outflow, again unresolved at the radio-jet scales, is also detected (Fotopoulou et al. 2019). In NGC1266, high-velocity H α is seen inside and near the spatially resolved jet, probed by its 1.4 and 5GHz emission (Davis et al. 2012). A nuclear molecular outflow, offset in positive and negative velocities along a similar orientation was detected in CO Alatalo et al. (2011). In NGC5643, an ionized outflow delineates the jet axis (Cresci et al. 2015), while a potential CO detection (Alonso-Herrero et al. 2018) is here treated as an upper limit.

The third group comprises sources in which the jet could be related to the outflow, because it spatially coincides with or extends in the same direction as the outflow. In NGC613, which is a spiral galaxy with a resolved radio jet and a nuclear outflow with an extremely high momentum rate ($\sim 400L_{\text{AGN}}/c$), an offset between the blueshifted and redshifted CO emission is seen in the jet direction (Audibert et al. 2019). In the merging system NGC3256, the southern nucleus shows a disk plus a bipolar jet radio map; an outflow is located at both jet edges (Sakamoto et al. 2014). Other galaxies with molecular outflows in the direction of large or small-scale jets comprise NGC1433 (Combes et al. 2013), NGC6764 (Leon et al. 2007), Circinus (Zschaechner et al. 2016; Harnett 1987), and Mrk273 (Cicone et al. 2014; González-Alfonso et al. 2017). In PKS1549-79, an [OIII] wind fills a trajectory gap between a massive CO nuclear outflow and the radio jet Oosterloo et al. (2019). In HE1353-1917, a spectacular [OIII] and H α wind that leaves the galactic disk at the point of a jet-cloud interaction could have a molecular counterpart, which we treat as an upper limit (Husemann et al. 2019a). In 3C273 the [OIII] kinematics show counter-motions with respect to the disk along the jet trail; a molecular arc perpendicular to the jet trail is associated with the cocoon Husemann et al. (2019b). We again treat it as an upper limit. Another source that can be included in this third group is NGC3100 (Ruffa et al. 2022), which is a lenticular galaxy with young, resolved radio jets (total linear extent ≈ 2 kpc). Here outflowing, optically thin molecular gas with very high excitation temperatures (i.e., $T_{\text{ex}} \gg 50$ K) is detected around the jet path, indicating that an ongoing jet-cold gas coupling is altering the physics and kinematics of the involved gas fraction.

In Figure 12, we plot the outflow kinetic energy vs. the jet power, as well as the outflow kinetic luminosity vs. the AGN radiation pressure, color coding galaxies based on the above-mentioned classification scheme. Outflow and galaxy properties are summarized in Table C.1. Outflow masses are consistently computed using an X_{CO} of $4 \times 10^{19} \text{ cm}^{-2} (\text{K km s}^{-1})^{-1}$ in all galaxies but IC5063. We find that in nearly all low-luminosity AGN there is either a certain or a plausible link between the jet and the outflow. The only exception is NGC4418, for which the presence of a radio jet is unclear (but cannot be ruled out) based on its clumpy and elongated 5GHz morphology (Varenius et al. 2014). Even at high AGN luminosities, certain galaxies have unambiguously jet-driven outflows. In all (low- and high-luminosity) AGN, momentum boosting would have been required to explain the observed outflow if it were originating from the AGN radiation pressure alone (Cicone et al. 2014). The energy deposition by the jet softens or revokes the need for momentum boosting, which occurs during an adiabatic expansion of a radiatively driven bubble of an AGN. It also reduces the need for alternative explanations to momentum boosting such as AGN variability. In the variability scenario, the ongoing outflows were driven by radiation during earlier, more luminous phases of AGN activity (Zubovas & Nar-

dini 2020). Instead, the jet could energetically fully sustain the outflows in these galaxies, as its power exceeds the outflow kinetic energy. To deduce the jet power, we used the observed 1.4 GHz flux of each galaxy as follows. The radio emission of the starburst (from its SNaE) was computed from its far-infrared dust emission (Ivison et al. 2010) and subtracted from the observed 1.4 GHz flux. The residual synchrotron luminosity was converted into a total jet power, in other words the combined mechanical power of the cavity dominated by hadrons and radiative power of the synchrotron dominated by leptons, following a widely used calibration (Birzan et al. 2008), which encapsulates that the jet power of the jet is typically dominated by the cavity power (Cavagnolo et al. 2010).

Table C.1: Outflow and AGN properties of galaxies with molecular outflows

Galaxy	z	V_{out} km s^{-1}	\dot{M}_{out} $M_{\odot} \text{ yr}^{-1}$	$\log(L_{\text{AGN}})$ erg s^{-1}	$F_{1.4\text{GHz}}$ Jy	$\log(P_{\text{jet}})$ erg s^{-1}
NGC1377	0.00578	110	5	42.93	<0.0015 ¹	<42.46
NGC1068	0.00379	150	28	43.94	4.85 ²	43.56
4C12.50	0.1217	800 ³	652 ³	45.7	5.1 ⁴	44.62*
NGC1433	0.0036	100	0.7	42.24	0.0034 ⁵	42.45
Mrk231	0.04217	700	350	45.72	0.31 ⁴	...
IC5063	0.011	300	10	44.3	1.87 ²	43.74
M51	0.002	100	11	43.79	1.4 ⁶	43.17**
Mrk1014	0.16311	268	93	45.29	0.0225 ¹	43.84
NGC1266	0.00719	177	11	43.31	0.115 ⁴	43.18
NGC5643	0.003999	500	85	42.91	0.203 ⁷	42.96
IRASF08572+3915	0.04311	800	403	45.72	0.0049 ¹	...
IRASF10565+2448	0.189	450	100	44.81	0.0576 ¹	...
IRASF11119+3257	0.06438	1000	203	46.2	0.106 ⁸	43.77
IRASF23365+3604	0.02448	450	57	44.67	0.0287 ⁴	...
NGC6240	0.123	400	267	45.38	0.427 ²	...
SDSSJ1356+1026	0.04256	500	118	46	0.49 ⁹	...
IRAS05189-2524	0.007268	491	219	44.47	0.0291 ¹	...
NGC4418	0.06764	134	19	43.81	0.0414 ⁴	...
IRASF14378-3651	0.030761	425	180	45.12	0.0349 ¹	...
IRAS13120-5453	0.08257	549	1115	44.35	0.065 ²	...
IRASF14348-1447	0.04295	450	420	44.59	0.018 ^{10 11}	...
NGC613	0.00495	300 ¹²	19 ¹²	42.6 ¹³	0.223 ²	43.18
ESO420-613	0.01205	379 ¹⁴	14 ¹⁴	44.0 ¹⁴	0.1 ¹⁴	43.25
PKS1549-79	0.15	600 ¹⁵	1733 ¹⁵	44.7 ²⁵	5.36 ¹⁶	44.69
3C273	0.15834	245 ²⁴	439 ²⁴	46.06 ²⁶	55 ¹	45.06***
HE1353-1917	0.03502	145 ¹⁷	22 ¹⁷	43.42 ¹⁸	0.0128 ¹	...
NGC6764	0.00807	170	1	42.23	0.113 ¹⁹	43.15
Circinus	0.0014	150	1	43.57	1.2 ²	42.89
Mrk273	0.03777	620	200	44.16	0.145 ¹	43.62
NGC3256S	0.00926	1400 ²¹	19 ²¹	42.04 ²⁰	0.0168 ^{****}	42.97
NGC3100	0.0088	200 ²²	0.12 ²²	42.78 ²²	0.5 ²³	43 ²²
NGC6328	0.014	150	3.1	42.11	0.32	42.35

Notes. are from Allison et al. (2014), unless otherwise indicated. For 4C12.50, properties are presented for the nuclear outflow component, as the extended components add little to the energetics (Fotopoulou et al. 2019). Likewise, the infrared luminosity fraction of the southern nucleus comes from resolved SF rates (Lira et al. 2002). The radio power, P_{jet} , (for the sources with a certain radio jet detection) is calculated as in Bîrzan et al. (2008) after the subtraction of the starburst contribution, as indicated in the text. Alternative radio power (P_{jet}) computations are as follows: (*) 43.96 for the synchrotron radiation (Fotopoulou et al. 2019), (**) 39.3 for the X-ray cavity (Urquhart et al. 2018), and (***) an averaged value of 43.86 Punsly & Kharb (2016). (****) To find the 1.4GHz flux fraction assigned to the southern nucleus of this galaxy merger, we used the information from spatially resolved 5 GHz data (Neff et al. 2003). ⁽¹⁾ Condon et al. (1998). ⁽²⁾ Allison et al. (2014). ⁽³⁾ Fotopoulou et al. (2019). ⁽⁴⁾ Baan & Klöckner (2006). ⁽⁵⁾ Ryder et al. (1996). ⁽⁶⁾ Dumas et al. (2011). ⁽⁷⁾ Condon et al. (1996). ⁽⁸⁾ Urrutia et al. (2009). ⁽⁹⁾ Greene et al. (2012). ⁽¹⁰⁾ Clemens et al. (2008). ⁽¹¹⁾ Clemens et al. (2010). ⁽¹²⁾ Audibert et al. (2019). ⁽¹³⁾ Davies et al. (2017). ⁽¹⁴⁾ Fernández-Ontiveros et al. (2020). ⁽¹⁵⁾ Oosterloo et al. (2019). ⁽¹⁶⁾ Drake et al. (2004). ⁽¹⁷⁾ Husemann et al. (2019a). ⁽¹⁸⁾ Shimizu et al. (2017). ⁽¹⁹⁾ Marvil et al. (2015). ⁽²⁰⁾ Ohyama et al. (2015). ⁽²¹⁾ Sakamoto et al. (2014). ⁽²²⁾ Ruffa et al. (2022). ⁽²³⁾ Ruffa et al. (2019). ⁽²⁴⁾ Husemann et al. (2019b). ⁽²⁵⁾ Lanz et al. (2016). ⁽²⁶⁾ Gruppioni et al. (2016)

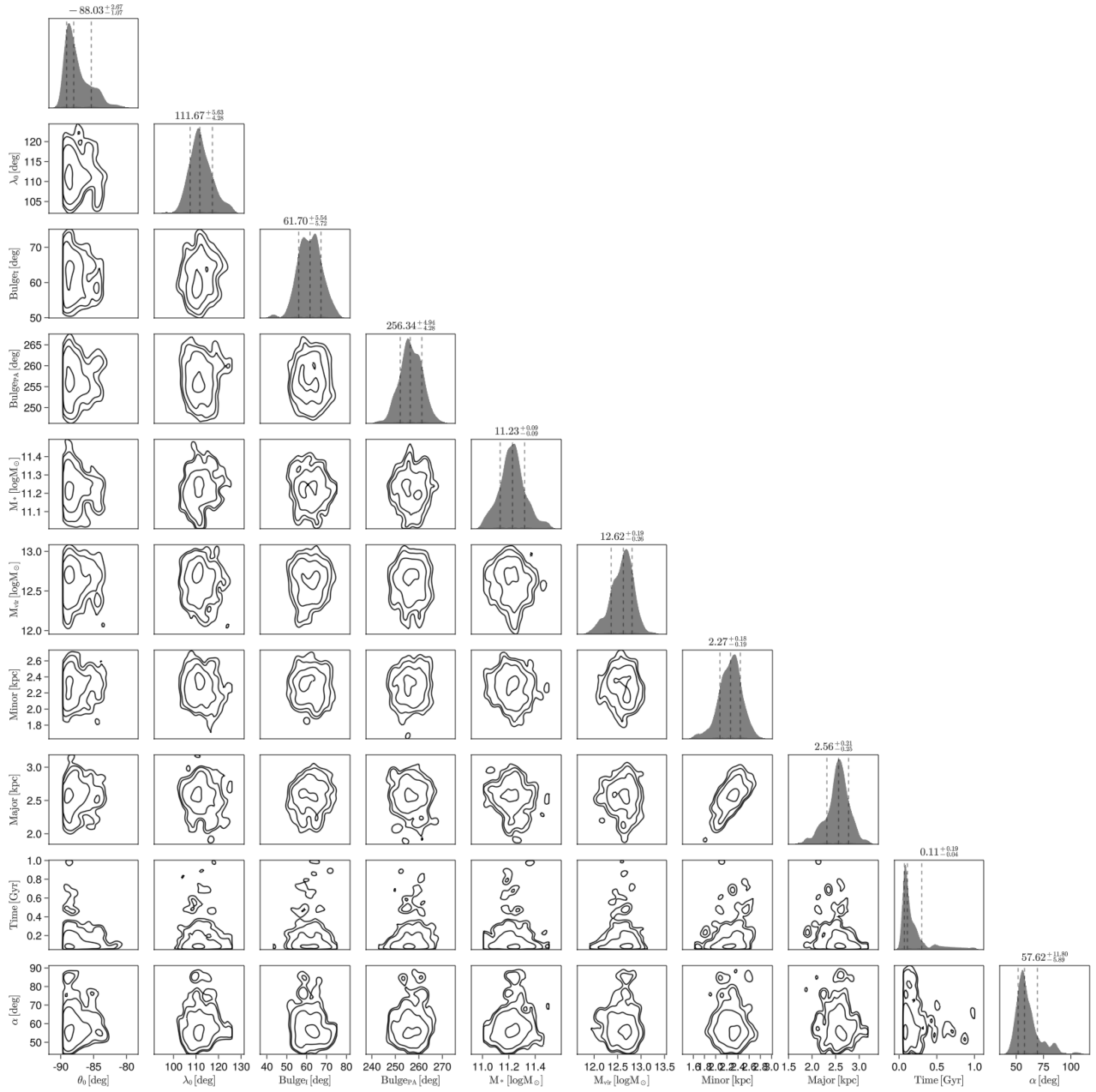


Fig. C.1: Corner plot of the parameters for the axisymmetric potential model.